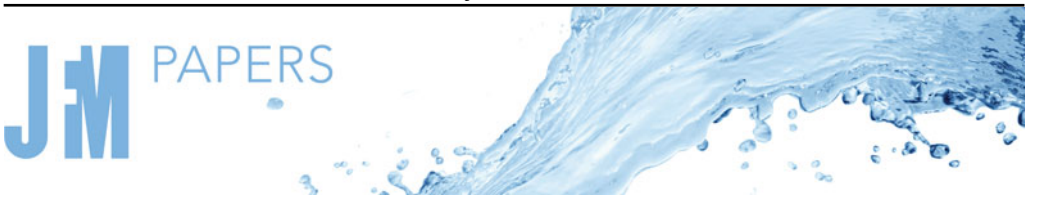
J. Fluid Mech. (2025), *vol.* 1019, A20, doi:10.1017/jfm.2025.10562



Interfacial wave coupling in an orbitally rotating cylinder

Yi-Fei Huang[1], **Ze Lyu**[1], **Juan-Cheng Yang**[2] **and Ming-Jiu Ni**[1]

[1]School of Engineering Science, University of Chinese Academy of Sciences, Beijing 100049, PR China

[2]State Key Laboratory for Strength and Vibration of Mechanical Structures, School of Aerospace Engineering, Xi'an Jiaotong University, Xi'an 710049, PR China

Corresponding authors: Juan-Cheng Yang, yangjc@xjtu.edu.cn; Ming-Jiu Ni, mjni@ucas.ac.cn

(Received 2 April 2025; revised 30 June 2025; accepted 6 August 2025)

This study explores interfacial waves in a three-layer fluid system, focusing on the coupling effects between the two interfaces. These effects include resonance induced by inertial coupling and damping caused by viscous coupling. A linear theoretical framework is developed to describe the coupled wave motion and evaluate the impact of interfacial coupling under viscous damping. Additionally, a semi-analytical model is introduced to accurately capture resonance frequency shifts and phase differences due to viscosity. The spiral structure of interfacial waves predicted by the models is confirmed experimentally using the background oriented Schlieren (BOS) method. Further, the model is validated by excellent agreement between theoretical predictions and ultrasonic measurements of wave amplitudes and phase differences. Finally, the study examines mechanical coupling and energy transfer between interfaces under external forcing, elucidating the formation of spiral waves. The accurate treatment of viscous boundary conditions by the semi-analytical model also enables its extension to multilayer fluid systems.

Key words: wave-structure interactions, surface gravity waves

1. Introduction

Interfacial waves are widespread in nature, such as sloshing (Faltinsen & Timokha 2009) induced by external forcing. Research on sloshing has historically focused on topics such as the transportation of liquid fuels during rocket flights, maritime transport, land transport of oil (Dodge *et al.* 2000) and liquefied natural gas (Abramson 1966). In recent years, new applications have rekindled interest in sloshing waves. On offshore oil platforms, surface wave-induced interface waves affect the crucial oil–water separation process, reducing static separation efficiency (Liu *et al.* 2022, 2023). Cell cultures and pharmaceutical production in biochemical engineering rely on interface wave-induced flow patterns to

© The Author(s), 2025. Published by Cambridge University Press.

https://doi.org/10.1017/jfm.2025.10562 Published online by Cambridge University Press

facilitate gas exchange and liquid mixing (Klöckner & Büchs 2012; Klöckner *et al.* 2014). Under controlled laboratory conditions, various patterns of Faraday waves (Kiyashko *et al.* 1996; Pucci *et al.* 2011; Bisswanger *et al.* 2024) are driven and applied in fields such as particle manipulation (Chen *et al.* 2014) and self-assembly of cells (Guex *et al.* 2021). In liquid metal batteries (LMBs), metal pad roll (MBR) instabilities can induce interface waves between liquid layers. These waves have the potential to short-circuit the thin electrolyte layer, damaging the LMBs (Horstmann, Weber & Weier 2018; Kelley & Weier 2018; Herreman *et al.* 2023).

By sloshing the container in a circular orbit, interfacial waves, which have hydrodynamic similarities to MPR waves, can be generated at the interface between two viscous fluid layers. Horstmann, Herreman & Weier (2020) developed a theoretical model for sloshing in a two-layer viscous fluid system, effectively describing gravity-capillary waves in orbitally shaken cylindrical containers. He constructed a set of irrotational wave equations based on potential flow theory with viscous damping used to represent energy dissipation. This approach enabled explicit calculations of the phase shift between the wave and the shaker, which has practical significance for the mixing efficiency of orbitally oscillating bioreactors. Additionally, Horstmann *et al.* (2019) used ultrasonic measurement techniques to obtain the amplitude and phase of the interfacial waves, validating their theoretical model. Based on this model, damping-induced spiral patterns were discovered and experimentally captured using the background oriented Schlieren (BOS) method (Horstmann *et al.* 2021). However, for LMBs consisting of three fluid layers, the viscous fluid interface coupling effects have not been studied to date. Due to the interface coupling, various instability modes have been discovered (Horstmann *et al.* 2018; Ward *et al.* 2019*a*; Herreman *et al.* 2023; Huang *et al.* 2024; Gong *et al.* 2025). However, studies on the orbital excitation of three-layer sloshing in viscous fluids remain limited. Moreover, current theoretical models cannot accurately capture the viscosity-induced frequency shifts (Horstmann *et al.* 2020) and phase differences (Reclari *et al.* 2014; Marcotte, Gallaire & Bongarzone 2023), which are crucial for understanding interface waves (Bongarzone *et al.* 2022). Therefore, a more general and precise theoretical model needs to be proposed.

Bauer & Eidel (1999) and Ibrahim (2005) proposed a semi-analytical model for implicitly solving the Navier–Stokes (N-S) equations, focusing on accurately satisfying the no-slip boundary condition at the sidewalls to analyse boundary layer effects. However, this method is computationally intensive and challenging to extend to multilayer fluid systems. Similar semi-analytical approaches have been applied to studies of Faraday waves. For example, Kumar & Tuckerman (1994) introduced a Floquet analysis model that rigorously satisfies interfacial boundary conditions, which Batson *et al.* (2013) validated experimentally for cases where sidewall effects are negligible (Ward *et al.* 2019*b*). Recently, Viola, Gallaire & Dollet (2017) studied sloshing surface waves in viscous fluids within Hele-Shaw cells. Their model uses gap-averaging to simplify boundary layer effects, followed by a Fourier series expansion of the N-S equations. This approach satisfies interfacial boundary conditions, and accurately predicts wave amplitude and phase. Based on these insights, we aim to develop a semi-analytical model for sloshing in multilayer viscous fluids within cylindrical containers.

In this paper, we develop an experimental system for three-layer fluid sloshing in a cylindrical container with ultrasound technology to capture interface positions and BOS to visualise interface patterns (§ 2). Based on Horstmann's work, a theoretical framework for orbitally excited three-layer sloshing is established to analyse the dynamic behaviour of waves in three-layer fluid systems. We derive wave equations based on potential flow theory with three-layer viscous damping and describe the phase shift between two waves

https://doi.org/10.1017/jfm.2025.10562 Published online by Cambridge University Press

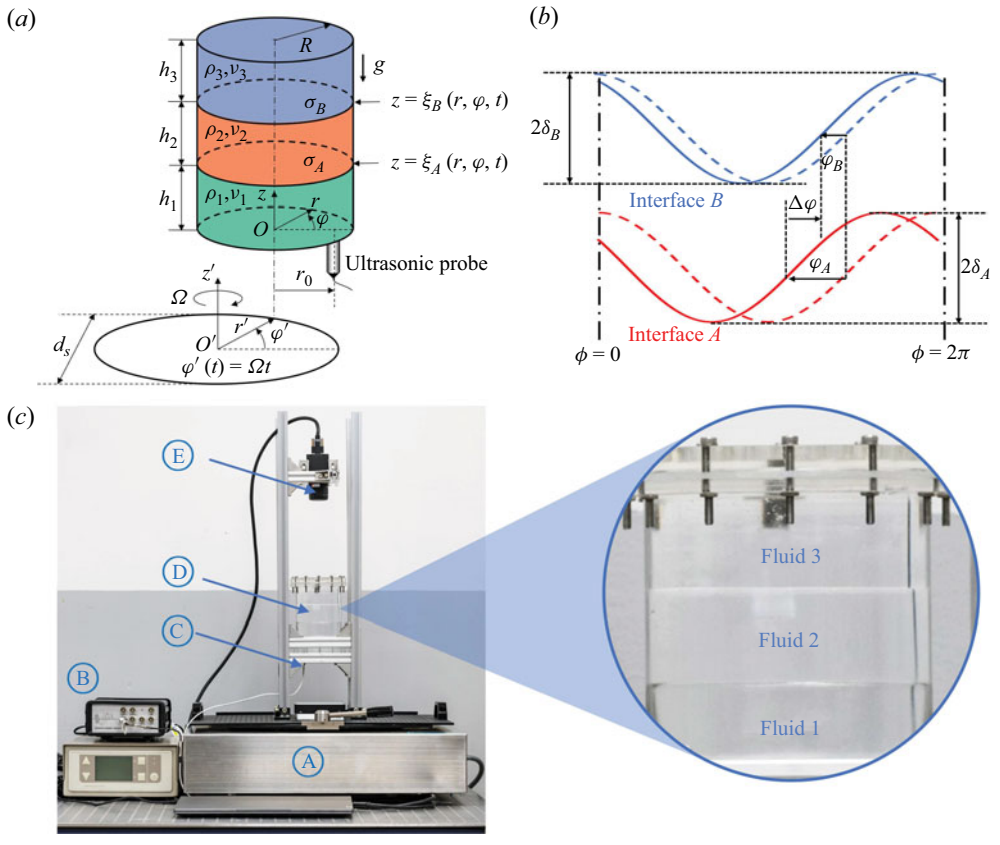


Figure 1. (*a*) Schematic diagram of an experimental system with three-layer fluid. (*b*) Typical interface waves during one period, where $\phi = \Omega t - \varphi$; $\Delta\varphi$ is the phase difference between two interface waves; φ_A and φ_B represent phase differences between interfaces and the shaker; δ_A and δ_B are the wave amplitudes of interfaces A and B. (*c*) Photographs of the experimental platform and three-layer stratification with **(A)** shaker, **(B)** power supply, **(C)** ultrasonic probe, **(D)** acrylic container and **(E)** camera.

for the first time. In addition, a semi-analytical model is obtained from the Fourier-expanded Navier–Stokes equations for more accurate theoretical predictions in § 3. We predict wave amplitudes and phases based on theoretical models and discuss energy transport (§ 4). Moreover, the theoretical results are validated by experimental findings, which reveal spiral structures in the three-layer fluid system (§ 5). Finally, our conclusions are presented in § 6.

2. Experimental platform

Circular orbit oscillations induce interface waves in a viscous fluid, allowing us to investigate the damping mechanisms of multi-layer stratified fluid interface waves. Similar to the experimental set-up of Horstmann *et al.* (2019), as shown in figure 1, we construct a physical test system with three-layer fluid. A cylindrical container of inner diameter $2R = 80$ mm and height $H = 100$ mm is filled to the brim with three immiscible liquids in layers. The bottom layer (fluid 1) thickness is fixed at $h_1 = 30$ mm with the thickness h_2 of the middle layer (fluid 2) and the thickness $h_3 = H - h_1 - h_2$ of the top layer (fluid 3). The three-layer fluid system (denoted as $j = 1, 2, 3$ for fluids 1, 2 and 3, respectively), with densities ρ_j, kinematic viscosities ν_j and thicknesses h_j, is supported by an aluminium

https://doi.org/10.1017/jfm.2025.10562 Published online by Cambridge University Press

frame and fixed on a Kuhner ES-X lab-shaker (500 mm × 420 mm). The diameter of the shaker, d_s, is 25 mm. The angular frequency $f = \Omega/2\pi$. In the cylindrical coordinate system $O(r, \varphi, z)$, gravity is represented by the acceleration, g, acting in the negative z-direction. The interface tension coefficient of interface A between fluids 1 and 2 is σ_A at $z = \xi_A(r, \varphi, z)$. Similarly, the interface tension coefficient of interface B between fluids 2 and 3 is σ_B at $z = \xi_B(r, \varphi, z)$. Following the assumption suggested by Horstmann *et al.* (2020), we neglect capillary forces acting on the contact line and assume a 90-degree contact angle between the interface and the cylindrical wall. The origin of the moving coordinate system $O(r, \varphi, z)$ is defined on a circle with a fixed point O' as the centre and d_s as the diameter. In the $O'(r', \varphi', z')$ coordinate system, point O moves uniformly around point O'. The velocity vector V_0 describing the orbital motion of the container can be expressed in the cylindrical coordinate system of the inertial reference frame $O'(r', \varphi', z')$ as $\boldsymbol{V}_0(t) = (-d_s\Omega \sin(\Omega t - \varphi')/2, d_s\Omega \cos(\Omega t - \varphi')/2, 0)$.

An Air|P|S system (i.e. of air/paraffin oil/silicone oil) is selected to measure simultaneously the amplitude and phase difference of the two fluid interfaces. The interfacial tension coefficient between air and paraffin oil is approximately 20 mN m^{-1}. The interfacial tension coefficient between paraffin oil and silicone oil is approximately 5 mN m^{-1}. The ultrasonic technique to measure the positions of the interfaces is based on time to flight. Further, we extend this measurement method to two fluid interfaces (Appendix A). Figure 1(*a*) shows that an ultrasonic probe with a centre frequency of 4 MHz and a diameter of 8 mm is positioned on the bottom surface at $r_0 = 30$ mm. We use multichannel pulsed ultrasonic Doppler velocimetry (MPUDV) (Pan *et al.* 2025) supplied by the University of Chinese Academy of Science (UCAS) for the acoustic measurements of interface wave motion. As shown in figure 1(*a*), the elevation of interface A (the interface between fluid 1 and fluid 2) above the base of the container is $\xi_A \approx c_1\Delta t_A/2$, where c_1 represents the speed of sound in fluid 1 and Δt_A is the time to travel from transmission to reception at interface A. The elevation of interface B above the base of the container is $\xi_B \approx \xi_A + c_2(\Delta t_B - \Delta t_A)/2$, where c_2 is the speed of sound in fluid 2 and Δt_B is the time to travel from transmission to reception at interface B. The amplitudes, δ_A and δ_B, and the phase difference, $\Delta\varphi$, of interface waves are obtained by ultrasonic measurement.

In addition, we select a P|S|G system (i.e. of paraffin oil/silicone oil/glycerol) to use the BOS method for measurements in our experiments. The interfacial tension coefficient between silicone oil (S) and glycerol (G) is approximately 18.2 mN m^{-1}. BOS is an optical method designed to measure the instantaneous topography of the interface between two transparent fluids, which has been applied to measure interface waves. The visual displacement of random speckle patterns through interface refraction is the theoretical basis of this method. The surface gradient field is determined by the apparent displacement between the refracted image and a reference image taken when the surface is flat. Following the work of Moisy, Rabaud & Salsac (2009), we can show that the virtual displacement $\delta\boldsymbol{r}$ reflects a weighted sum of the gradients at the two interfaces (Appendix B), $(1 - n_2/n_1)h_1\nabla\xi_A + (1 - n_3/n_2)(h_1 + h_2)\nabla\xi_B \sim -\delta\boldsymbol{r}$, where n_j represents the refractive index of the fluid j. As shown in figure 1, a diffuse backlight LED array (150 mm × 150 mm) is placed below the container. Additionally, a random dot pattern of approximately 20 dots mm^{-2}, generated using the PIVMat Toolbox, is placed between the container and the LED array. We captured images of the pattern at a resolution of 0.06 mm pixel^{-1} with an industrial camera (U3P630-H), positioned approximately 200 mm above the container at a frame rate of 70 fps. The system is placed on the shaker such that the camera and light source moved synchronously with the

https://doi.org/10.1017/jfm.2025.10562 Published online by Cambridge University Press

experimental set-up. Finally, digital image correlation (DIC) is performed on the point patterns captured during motion and the stationary point patterns using MATLAB.

3. Theory

The incompressible N-S equations and boundary conditions for the viscous interface wave mechanics of three-layer fluid systems are listed in Appendix C in terms of velocity $\boldsymbol{v}_j$, pressure p_j, density ρ_j and kinematic viscosity ν_j $(j = 1, 2, 3)$. We define a small parameter $\epsilon = 2Fr$, where $Fr = d_s\Omega^2/g$ is the Froude number, and perform a perturbation-based asymptotic expansion as follows:

$$\begin{aligned}
&\boldsymbol{v}_j = \boldsymbol{u}_j + \mathrm{O}(\epsilon^2),\\
&p_j = p_{j,0} + \rho_j \frac{d_s\Omega^2 r}{2}\cos(\Omega t - \varphi) + \hat{p}_j + \mathrm{O}(\epsilon^2),\\
&\xi_A = h_1 + \eta_A + \mathrm{O}(\epsilon^2),\\
&\xi_B = h_1 + h_2 + \eta_B + \mathrm{O}(\epsilon^2).
\end{aligned} \tag{3.1}$$

From the perturbation expansion, we obtain the first-order incompressible N-S equations (3.2*b*),

$$\nabla \cdot \boldsymbol{u}_j = 0, \tag{3.2a}$$

$$\frac{\partial \boldsymbol{u}_j}{\partial t} = -\frac{1}{\rho_j}\nabla \hat{p}_j + \nu_j \nabla^2 \boldsymbol{u}_j, \tag{3.2b}$$

and corresponding boundary conditions (3.3),

$$\text{Wall}: \ \boldsymbol{u}_j\big|_{z=0 \,\|\, z=\sum_1^3 h_j \,\|\, r=R} = 0, \tag{3.3a}$$

$$\text{Interface } A: \ \boldsymbol{u}_1 \cdot \boldsymbol{e}_z|_{z=h_1} = \boldsymbol{u}_2 \cdot \boldsymbol{e}_z|_{z=h_1} = \frac{\partial \eta_A}{\partial t}, \tag{3.3b}$$

$$\boldsymbol{u}_1 \cdot \boldsymbol{e}_x|_{z=h_1} = \boldsymbol{u}_2 \cdot \boldsymbol{e}_x|_{z=h_1}, \tag{3.3c}$$

$$\boldsymbol{u}_1 \cdot \boldsymbol{e}_y\big|_{z=h_1} = \boldsymbol{u}_2 \cdot \boldsymbol{e}_y\big|_{z=h_1}, \tag{3.3d}$$

$$\boldsymbol{e}_z \cdot \left(\tau_{1,ls} - \tau_{2,ls}\right) \cdot \boldsymbol{e}_z\big|_{z=h_1} = \sigma_A \nabla^2 \eta_A, \tag{3.3e}$$

$$\boldsymbol{e}_z \cdot \left(\tau_{1,ls} - \tau_{2,ls}\right) \cdot \boldsymbol{e}_x\big|_{z=h_1} = 0, \tag{3.3f}$$

$$\boldsymbol{e}_z \cdot \left(\tau_{1,ls} - \tau_{2,ls}\right) \cdot \boldsymbol{e}_y\big|_{z=h_1} = 0, \tag{3.3g}$$

$$\text{Interface } B: \ \boldsymbol{u}_2 \cdot \boldsymbol{e}_z|_{z=h_1+h_2} = \boldsymbol{u}_3 \cdot \boldsymbol{e}_z|_{z=h_1+h_2} = \frac{\partial \eta_B}{\partial t}, \tag{3.3h}$$

$$\boldsymbol{u}_2 \cdot \boldsymbol{e}_x|_{z=h_1+h_2} = \boldsymbol{u}_3 \cdot \boldsymbol{e}_x|_{z=h_1+h_2}, \tag{3.3i}$$

$$\boldsymbol{u}_2 \cdot \boldsymbol{e}_y\big|_{z=h_1+h_2} = \boldsymbol{u}_3 \cdot \boldsymbol{e}_y\big|_{z=h_1+h_2}, \tag{3.3j}$$

$$\boldsymbol{e}_z \cdot \left(\tau_{2,ls} - \tau_{3,ls}\right) \cdot \boldsymbol{e}_z\big|_{z=h_1+h_2} = \sigma_B \nabla^2 \eta_B, \tag{3.3k}$$

$$\boldsymbol{e}_z \cdot \left(\tau_{2,ls} - \tau_{3,ls}\right) \cdot \boldsymbol{e}_x\big|_{z=h_1+h_2} = 0, \tag{3.3l}$$

$$\boldsymbol{e}_z \cdot \left(\tau_{2,ls} - \tau_{3,ls}\right) \cdot \boldsymbol{e}_y\big|_{z=h_1+h_2} = 0, \tag{3.3m}$$

with $\tau_{j,ls}$ as the stress tensor of fluid j.

https://doi.org/10.1017/jfm.2025.10562 Published online by Cambridge University Press

	Density (kg m^{-3})	Kinematic viscosity (cst)	Thickness (mm)
Air|P|S system			
Air	1.29	14.8	$70 - h_2$
Paraffin oil (P)	860	40	h_2
Silicone oil (S)	970	50 or 500	30
P|S|G system			
Paraffin oil (P)	860	40	40
Silicone oil (S)	970	50	30
Glycerol (G)	1297	1190	30

Table 1. Experimental parameters of the two sets of experiments.

3.1. *The modified model*

In practice, it is not easy to find analytical solutions for the dynamics of viscous waves. In the past, potential theory was applied in many studies to approximate the velocity field based on inviscid, irrotational and incompressible flow assumptions. Nevertheless, potential theory has successfully predicted non-resonant sloshing (Ibrahim 2005). As described by Faltinsen & Timokha (2009), although potential flow theory is strictly only applicable to irrotational flow, it allows the inclusion of viscous damping rates in the model equations. In this way, provided the wave amplitude is sufficiently small, the modified model accounts for linear and weakly nonlinear phenomena (Faltinsen & Timokha 2009). Horstmann *et al.* (2020) proposed a corresponding modified model in a two-layer viscous fluid system, adding the explicit viscous damping rates in cylindrical containers developed by Herreman *et al.* (2019). Similarly, a corresponding modified model can also be derived based on explicit damping rates for three-layer viscous fluid cylindrical containers, as presented by Herreman *et al.* (2023). However, the coupling effects between two fluid interfaces need to be evaluated for a three-layer fluid system. We established this model based on Horstmann's theoretical work (Horstmann *et al.* 2020, 2021; Horstmann 2021).

3.1.1. *Potential theory*

Based on potential flow theory (ignoring viscosity), the velocity field $\boldsymbol{u}_j$ can be represented by a potential function Φ_j. The velocity potential and interface wave functions should have the following functional forms to satisfy the slip condition at walls and interfaces:

$$\eta_A(r,\phi) = \sum_{n=1}^{\infty} \beta_{A,n}(\phi) \frac{J_1\left(k_{1,n} r\right)}{J_1\left(k_{1,n} R\right)}, \tag{3.4a}$$

$$\eta_B(r,\phi) = \sum_{n=1}^{\infty} \beta_{B,n}(\phi) \frac{J_1\left(k_{1,n} r\right)}{J_1\left(k_{1,n} R\right)}, \tag{3.4b}$$

$$\Phi_1(r,\phi,z) = \sum_{n=1}^{\infty} \frac{\Omega \dot{\beta}_{A,n}}{k_{1,n}} \frac{\cosh k_{1,n} z}{\sinh k_{1,n} h_1} \frac{J_1\left(k_{1,n} r\right)}{J_1\left(k_{1,n} R\right)}, \tag{3.4c}$$

$$\Phi_2(r,\phi,z) = -\sum_{n=1}^{\infty} \left(\frac{\Omega \dot{\beta}_{A,n}}{k_{1,n}} \frac{\cosh k_{1,n}(z-h_1-h_2)}{\sinh k_{1,n} h_2} - \frac{\dot{\Omega} \beta_{B,n}}{k_{1,n}} \frac{\cosh k_{1,n}(z-h_1)}{\sinh k_{1,n} h_2} \right) \frac{J_1(k_{1,n} r)}{J_1(k_{1,n} R)}, \tag{3.4d}$$

https://doi.org/10.1017/jfm.2025.10562 Published online by Cambridge University Press

$$\Phi_3(r,\phi,z) = -\sum_{n=1}^{\infty} \frac{\Omega\dot{\beta}_{B,n}}{k_{1,n}} \frac{\cosh k_{1,n}\,(z-h_1-h_2-h_3)}{\sinh k_{1,n}h_3} \frac{J_1\left(k_{1,n}r\right)}{J_1\left(k_{1,n}R\right)}, \tag{3.4e}$$

with, $k_{1,n} = \varepsilon_{1,n}/R$, $J_1'(\varepsilon_{1,n}) = 0$, $\phi = \Omega t - \varphi$, where the quantities η_A and η_B denote the first-order approximations of the interfacial waves at interfaces A and B, respectively, with $J_1(k_{1,n}r)$ representing the Bessel function of the first kind of order one. The interfacial dynamic boundary conditions (3.3*e*, 3.3*k*) may be simplified to give

$$\rho_1\Omega\frac{\mathrm{d}\Phi_1}{\mathrm{d}\phi}\bigg|_{z=h_1} - \rho_2\Omega\frac{\mathrm{d}\Phi_2}{\mathrm{d}\phi}\bigg|_{z=h_1} + \left((\rho_1-\rho_2)g - \sigma_A\nabla^2_{(r,\varphi)}\right)$$
$$\eta_A = (\rho_1-\rho_2)\frac{d_s\Omega^2 r}{2}\cos\phi, \tag{3.5a}$$
$$\rho_2\Omega\frac{\mathrm{d}\Phi_2}{\mathrm{d}\phi}\bigg|_{z=h_1+h_2} - \rho_3\Omega\frac{\mathrm{d}\Phi_2}{\mathrm{d}\phi}\bigg|_{z=h_1+h_2} + \left((\rho_2-\rho_3)g - \sigma_B\nabla^2_{(r,\varphi)}\right)$$
$$\eta_B = (\rho_2-\rho_3)\frac{d_s\Omega^2 r}{2}\cos\phi, \tag{3.5b}$$

with $\nabla^2_{(r,\varphi)} = (\partial^2/\partial r^2) + (1/r)(\partial/\partial r) + (1/r^2)(\partial^2/\partial\theta^2)$. Substituting (3.4) into (3.5), we obtain

$$\frac{J_1\left(k_{1,n}r\right)}{J_1\left(k_{1,n}R\right)}\left(\Omega^2\frac{\mathrm{d}^2\beta_{A,n}}{\mathrm{d}\phi^2} - \rho_{A,n}\Omega^2\frac{\mathrm{d}^2\beta_{B,n}}{\mathrm{d}\phi^2} + \Omega^2_{A,n}\beta_{A,n}\right)$$
$$= \frac{d_s}{2}\frac{(\rho_1-\rho_2)\,k_{1n}\Omega^2 r}{\rho_1\coth(k_{1n}h_1) + \rho_2\coth(k_{1n}h_2)}\sin\phi, \tag{3.6a}$$
$$\frac{J_1\left(k_{1,n}r\right)}{J_1\left(k_{1,n}R\right)}\left(\Omega^2\frac{\mathrm{d}^2\beta_{B,n}}{\mathrm{d}\phi^2} - \rho_{B,n}\Omega^2\frac{\mathrm{d}^2\beta_{A,n}}{\mathrm{d}\phi^2} + \Omega^2_{B,n}\beta_{B,n}\right)$$
$$= \frac{d_s}{2}\frac{(\rho_2-\rho_3)\,k_{1n}\Omega^2 r}{\rho_2\coth(k_{1n}h_2) + \rho_3\coth(k_{1n}h_3)}\sin\phi, \tag{3.6b}$$

with

$$\rho_{A,n} = \frac{\rho_2\,\mathrm{csch}(k_{1,n}h_2)}{\rho_1\coth(k_{1,n}h_1) + \rho_2\coth(k_{1,n}h_2)},\ \rho_{B,n} = \frac{\rho_2\,\mathrm{csch}(k_{1,n}h_2)}{\rho_2\coth(k_{1,n}h_2) + \rho_3\coth(k_{1,n}h_3)},$$
$$\Omega^2_{A,n} = \frac{(\rho_1-\rho_2)gk_{1,n} + \sigma_A k^3_{1,n}}{\rho_1\coth(k_{1,n}h_1) + \rho_2\coth(k_{1,n}h_2)},\ \Omega^2_{B,n} = \frac{(\rho_2-\rho_3)gk_{1,n} + \sigma_B k^3_{1,n}}{\rho_2\coth(k_{1,n}h_2) + \rho_3\coth(k_{1,n}h_3)}, \tag{3.7}$$

where $\Omega_{A,n}$ and $\Omega_{B,n}$ represent the natural frequencies (Huang *et al.* 2024) associated with interface A and interface B, respectively. The parameters $\rho_{A,n}$ and $\rho_{B,n}$ quantify the coupling strength between the two interfacial waves. When the shallow assumption $k_{1,n}h_j \ll 1$ is satisfied,

$$\rho_{A,n} \approx \frac{1}{1+(h_2/h_1)\,(\rho_1/\rho_2)}, \quad \rho_{B,n} \approx \frac{1}{1+(h_2/h_3)\,(\rho_3/\rho_2)} \tag{3.8}$$

and

$$\frac{\rho_{A,n}}{\rho_{B,n}} \approx \frac{1+(\rho_3/\rho_2)\,(h_2/h_3)}{1+(\rho_1/\rho_2)\,(h_2/h_1)}. \tag{3.9}$$

https://doi.org/10.1017/jfm.2025.10562 Published online by Cambridge University Press

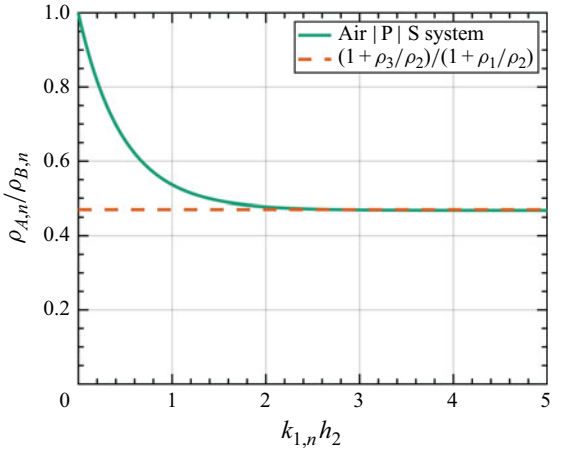


Figure 2. Variation of the coupling coefficient $\rho_{A,n}/\rho_{B,n}$ with $k_{1,n}h_2$ in the Air|P|S system.

Furthermore, when $h_2 \to 0$, $\lim_{h_2\to 0}(\rho_{A,n}/\rho_{B,n}) \approx 1$ is obtained, indicating a strong interfacial coupling effect.

When the deep assumption $k_{1,n}h_j \gg 1$ is satisfied,

$$\rho_{A,n} \approx 0, \quad \rho_{B,n} \approx 0 \tag{3.10}$$

and

$$\frac{\rho_{A,n}}{\rho_{B,n}} \approx \frac{1+\rho_3/\rho_2}{1+\rho_1/\rho_2}, \tag{3.11}$$

which indicate a weak interfacial coupling effect.

Therefore, the closer $\rho_{A,n}/\rho_{B,n}$ is to one, the stronger the interfacial coupling effect; conversely, as $\rho_{A,n}/\rho_{B,n}$ approaches $(1+\rho_3/\rho_2)/(1+\rho_1/\rho_2)$, the coupling becomes weaker. To illustrate this intuitively, we take the Air|P|S system as an example and plot the variation of $\rho_{A,n}/\rho_{B,n}$ concerning $k_{1,n}h_2$ in figure 2.

From the orthogonality of the Bessel function $J_1(k_{1,n}r)$, (3.6) is reduced to

$$\frac{\mathrm{d}^2\beta_{A,n}}{\mathrm{d}\phi^2} - \rho_{A,n}\frac{\mathrm{d}^2\beta_{B,n}}{\mathrm{d}\phi^2} + \frac{\Omega_{A,n}^2}{\Omega^2}\beta_{A,n} = F_{A,n}d_s\sin\phi, \tag{3.12a}$$

$$\frac{\mathrm{d}^2\beta_{B,n}}{\mathrm{d}\phi^2} - \rho_{B,n}\frac{\mathrm{d}^2\beta_{A,n}}{\mathrm{d}\phi^2} + \frac{\Omega_{B,n}^2}{\Omega^2}\beta_{B,n} = F_{B,n}d_s\sin\phi, \tag{3.12b}$$

where

$$\begin{aligned} F_{A,n} &= \frac{(\rho_1-\rho_2)\,k_{1,n}R}{\left(\rho_1\coth k_{1,n}h_1 + \rho_2\coth k_{1,n}h_2\right)\left(\varepsilon_{1,n}^2-1\right)J_1\left(k_{1,n}R\right)}, \\ F_{B,n} &= \frac{(\rho_2-\rho_3)\,k_{1,n}R}{\left(\rho_2\coth k_{1,n}h_2 + \rho_3\coth k_{1,n}h_3\right)\left(\varepsilon_{1,n}^2-1\right)J_1\left(k_{1,n}R\right)}. \end{aligned} \tag{3.13}$$

The coefficients $F_{A,n}$ and $F_{B,n}$ quantify the influence of density stratification on the wave amplitudes at interfaces A and B, respectively, in a cylindrical container with finite fluid

https://doi.org/10.1017/jfm.2025.10562 Published online by Cambridge University Press

depth. As $h_j \to \infty$, $F_{A,n}$ and $F_{B,n}$ can be approximated as

$$F_{A,n} \approx \frac{A_{1,2} k_{1,n} R}{\left(\varepsilon_{1,n}^2 - 1\right) J_1\left(k_{1,n} R\right)}, \quad F_{B,n} \approx \frac{A_{2,3} k_{1,n} R}{\left(\varepsilon_{1,n}^2 - 1\right) J_1\left(k_{1,n} R\right)}, \tag{3.14}$$

where $A_{1,2} = (\rho_1 - \rho_2)/(\rho_1 + \rho_2)$ denotes the Atwood number between fluid 1 and fluid 2, and $A_{2,3} = (\rho_2 - \rho_3)/(\rho_2 + \rho_3)$ denotes the Atwood number between fluid 2 and fluid 3.

3.1.2. *Viscous damping*

Herreman *et al.* (2023) carried out a detailed study of the viscous damping terms in a three-layer fluid system, starting with the energy equation,

$$\begin{aligned} &\underbrace{\frac{\mathrm{d}}{\mathrm{d}t} \sum_{j=1,2,3} \frac{1}{2} \int_{V_j} \rho_j \left\| \boldsymbol{u}_j \right\|^2 \mathrm{d}V}_{E_c} + \\ &\underbrace{\frac{\mathrm{d}}{\mathrm{d}t} \int_{S_A} \left[\frac{1}{2} \left(\rho_2 - \rho_1\right) g \xi_A^2 + \sigma_A \sqrt{1 + \left\| \nabla \xi_A \right\|^2} \right] \mathrm{d}S + \int_{S_B} \left[\frac{1}{2} \left(\rho_3 - \rho_2\right) g \xi_B^2 + \sigma_B \sqrt{1 + \left\| \nabla \xi_B \right\|^2} \right] \mathrm{d}S}_{E_p} = \\ &\underbrace{- \sum_{j=1,2,3} 2 \rho_j \nu_j \int_{V_j} \varepsilon_j : \varepsilon_j \, \mathrm{d}V}_{D}, \end{aligned} \tag{3.15}$$

with kinetic energy E_c, potential energy E_p, viscous dissipation energy D and the shear rate tensor $\boldsymbol{\varepsilon}_j = (\partial u_{j,m}/\partial x_n + \partial u_{j,n}/\partial x_m)/2$. The simplification of viscous dissipation energy D leads to the following expression:

$$D = \underbrace{- \sum_{j=1,2,3} \rho_j \nu_j \int_{V_j} \left\| \nabla \times \boldsymbol{u}_j \right\|^2 \mathrm{d}V}_{D'} \underbrace{-2 \sum_{j=1,2,3} \rho_j \nu_j \int_{V_j} \nabla \cdot \left(\left(\boldsymbol{u}_j \cdot \nabla \right) \boldsymbol{u}_j \right) \mathrm{d}V}_{D''}. \tag{3.16}$$

In this context, the main contributions come from the boundary layer (D') and the fluid bulk (D''). The viscous attenuation surface wave field and the interface displacement are $\boldsymbol{u}_j \sim \mathrm{e}^{-\lambda t}$, $\eta \sim \mathrm{e}^{-\lambda t}$.

According to Herreman *et al.* (2023), it can be observed that viscous damping consists of three components: wall damping λ^{BL}, interface damping λ^{IL} and internal fluid damping λ^{Int}. Here, $\lambda = \lambda^{BL} + \lambda^{IL} + \lambda^{Int}$, with λ^{BL}, $\lambda^{IL} \sim k$ and $\lambda^{Int} \sim k^2$. Kumar & Tuckerman (1994) have provided a solution for λ^{Int}. As for the viscous dissipation energy in the fluid body, D'' can be approximated as

$$\begin{aligned} D'' &= -2 \sum_{j=1,2,3} \rho_j \nu_j \int_{V_j} \nabla \cdot \left(\left(\boldsymbol{u}_j \cdot \nabla \right) \boldsymbol{u}_j \right) \mathrm{d}V \\ &= -2 \sum_{j=1,2,3} \rho_j \nu_j \int_{V_j} \frac{\partial u_{i,k}}{\partial x_j} \frac{\partial u_{i,j}}{\partial x_k} \mathrm{d}V \approx -2 \sum_{j=1,2,3} \rho_j \nu_j \int_{V_j} \left(\frac{\partial^2 \Phi_j}{\partial x_j \partial x_k} \right)^2 \mathrm{d}V, \end{aligned} \tag{3.17}$$

https://doi.org/10.1017/jfm.2025.10562 Published online by Cambridge University Press

where Φ_j is the potential function of fluid j. Thus, we obtain the internal damping

$$\lambda^{Int} = \frac{\sum_{j=1}^{3} \int \mu_j \left(\frac{\partial^2 \Phi_j}{\partial x_j \partial x_k}\right)^2 \mathrm{d}V_j}{\sum_{j=1}^{3} \int \rho_j \left(\frac{\partial \Phi_j}{\partial x_j}\right)^2 \mathrm{d}V_j}$$

$$= \frac{\begin{array}{c} 2k_{1,n}^2\Big(\epsilon^2\rho_1 v_1 \coth\left(h_1 k_{1,n}\right) + \left(1+\epsilon^2\right)\rho_2 v_2 \coth\left(h_2 k_{1,n}\right) \\ +\rho_3 v_3 \coth\left(h_3 k_{1,n}\right) - 2\epsilon\rho_2 v_2 \operatorname{csch}\left(h_2 k_{1,n}\right)\Big) \end{array}}{\begin{array}{c} \epsilon^2\rho_1 \coth\left(h_1 k_{1,n}\right) + \left(1+\epsilon^2\right)\rho_2 \coth\left(h_2 k_{1,n}\right) \\ +\rho_3 \coth\left(h_3 k_{1,n}\right) - 2\epsilon\rho_2 \operatorname{csch}\left(h_2 k_{1,n}\right) \end{array}}, \tag{3.18}$$

with $\epsilon_{\pm} = a_n \pm \sqrt{a_n^2 + b_n}$, $a_n = (1/2)(1/\rho_{B,n} - (\rho_2 - \rho_3)/(\rho_{A,n}(\rho_1 - \rho_2)))$, $b_n = (\rho_2 - \rho_3)/(\rho_1 - \rho_2)$. Since the frequency range investigated in this study closely matches the natural frequency corresponding to the (-) mode, we adopt the value of ϵ_-. Note that λ^{BL} and λ^{IL} have been determined by Herreman *et al.* (2023). Here, $\lambda^{BL} = \lambda_1^{BL} + \lambda_2^{BL} + \lambda_3^{BL}$, where the contributions from the wall boundary layers are

$$\lambda_1^{BL} = \frac{\sqrt{2}}{4}\frac{1}{k_{1,n}R}\frac{\rho_1\Omega^2\sqrt{v_1\Omega}}{g\left(\rho_2 - \rho_3 + \epsilon^2\left(\rho_1 - \rho_2\right)\right)}$$
$$\times\ \epsilon^2\left[k_{1,n}\left(R - h_1\right)\operatorname{csch}^2\left(k_{1,n}h_1\right) + \frac{k_{1,n}^2R^2 + 1}{k_{1,n}^2R^2 - 1}\coth\left(k_{1,n}h_1\right)\right],$$

$$\lambda_2^{BL} = -\frac{\sqrt{2}}{4}\frac{1}{k_{1,n}R}\frac{\rho_2\Omega^2\sqrt{v_2\Omega}}{g\left(\rho_2 - \rho_3 + \epsilon^2\left(\rho_1 - \rho_2\right)\right)}$$
$$\times\ \left(\epsilon^2 + 1\right)\left(k_{1,n}h_2\operatorname{csch}^2\left(k_{1,n}h_2\right) - \frac{k_{1,n}^2R^2 + 1}{k_{1,n}^2R^2 - 1}\coth\left(k_{1,n}h_2\right)\right)$$
$$+\ \frac{\sqrt{2}}{2}\frac{1}{k_{1,n}R}\frac{\epsilon\rho_2\Omega^2\sqrt{v_2\Omega}}{g\left(\rho_2 - \rho_3 + \epsilon^2\left(\rho_1 - \rho_2\right)\right)}$$
$$\times\ \left(k_{1,n}h_2\coth\left(k_{1,n}h_2\right)\operatorname{csch}\left(k_{1,n}h_2\right) - \frac{k_{1,n}^2R^2 + 1}{k_{1,n}^2R^2 - 1}\operatorname{csch}\left(k_{1,n}h_2\right)\right),$$

$$\lambda_3^{BL} = \frac{\sqrt{2}}{4}\frac{1}{k_{1,n}R}\frac{\rho_3\Omega^2\sqrt{v_3\Omega}}{g\left(\rho_2 - \rho_3 + \epsilon^2\left(\rho_1 - \rho_2\right)\right)}$$
$$\times\ \left[k_{1,n}\left(R - h_3\right)\operatorname{csch}^2\left(k_{1,n}h_3\right) + \frac{k_{1,n}^2R^2 + 1}{k_{1,n}^2R^2 - 1}\coth\left(k_{1,n}h_3\right)\right]. \tag{3.19}$$

The sum damping of contributions from the interfacial boundary layers is

$$\lambda^{IL} = \frac{\sqrt{2}}{4}\frac{\Omega^2\sqrt{\Omega}}{g(\rho_2 - \rho_3 + \epsilon^2(\rho_1 - \rho_2))}\sum_{j=1,2}\Lambda_{jj+1}^2\left(\frac{1}{\rho_j\sqrt{v_j}} + \frac{1}{\rho_{j+1}\sqrt{v_{j+1}}}\right)^{-1}, \tag{3.20}$$

https://doi.org/10.1017/jfm.2025.10562 Published online by Cambridge University Press

with

$$\begin{aligned}\Lambda_{12} &= \epsilon(\coth(k_{1,n}h_1) + \coth(k_{1,n}h_2)) - \operatorname{csch}(k_{1,n}h_2),\\ \Lambda_{23} &= (\coth(k_{1,n}h_2) + \coth(k_{1,n}h_3)) - \epsilon\operatorname{csch}(k_{1,n}h_2).\end{aligned} \tag{3.21}$$

Usually, interface coupling effects exist in inertial terms. The strength of these coupling effects depends on $\rho_{A,n}$ and $\rho_{B,n}$. However, it is necessary to make corrections for the interface coupling effects caused by viscosity, because the motion contributes to inertial and viscous forces. Therefore, the effect of interfacial coupling is also considered when viscosity correction terms with Herreman's viscous decay rate λ (Herreman *et al.* 2023) are added. The following modified equations for the three-layer fluid system have been derived:

$$\underbrace{\frac{\mathrm{d}^2\beta_{A,n}}{\mathrm{d}\phi^2} - \rho_{A,n}\frac{\mathrm{d}^2\beta_{B,n}}{\mathrm{d}\phi^2}}_{\text{Inertial term}} + \underbrace{2\Upsilon\frac{\mathrm{d}\beta_{A,n}}{\mathrm{d}\phi} - 2\rho_{A,n}\Upsilon\frac{\mathrm{d}\beta_{B,n}}{\mathrm{d}\phi}}_{\text{Viscous term}} + \underbrace{\frac{\Omega_{A,n}^2}{\Omega^2}\beta_{A,n}}_{\text{Restoring term}} \underbrace{-F_{A,n}d_s\sin\phi}_{\text{Excitation term}} = 0, \tag{3.22a}$$

$$\underbrace{\frac{\mathrm{d}^2\beta_{B,n}}{\mathrm{d}\phi^2} - \rho_{B,n}\frac{\mathrm{d}^2\beta_{A,n}}{\mathrm{d}\phi^2}}_{\text{Inertial term}} + \underbrace{2\Upsilon\frac{\mathrm{d}\beta_{B,n}}{\mathrm{d}\phi} - 2\rho_{B,n}\Upsilon\frac{\mathrm{d}\beta_{A,n}}{\mathrm{d}\phi}}_{\text{Viscous term}} + \underbrace{\frac{\Omega_{B,n}^2}{\Omega^2}\beta_{B,n}}_{\text{Restoring term}} \underbrace{-F_{B,n}d_s\sin\phi}_{\text{Excitation term}} = 0, \tag{3.22b}$$

where $\Upsilon = \lambda/\Omega$ describes the ratio of viscous force to inertial force.

Equation (3.22) are equilibrium equations that describe the dynamics of interfaces A and B. The two equations are coupled through interfacial coupling coefficients. The viscous contribution is introduced via a dissipation rate, representing energy loss due to viscosity. The restoring term accounts for the combined effects of gravity and interfacial tension, providing the 'elastic response' of the interface, while the external term models the forcing induced by the orbital motion of the container. In two-layer systems with low viscosity, it is appropriate to model the viscous effect by adding a corrective term of the form $\Upsilon\,\mathrm{d}\beta_{A,n}/\mathrm{d}\phi$, ensuring that the energy dissipation rate matches Υ. However, this single correction is insufficient in a three-layer system with finite viscosity. The interfacial coupling alters the decay characteristics, and the modified system no longer exhibits a decay rate equal to Υ. To rectify this, an additional term $2\rho_{A,n}\Upsilon\,\mathrm{d}\beta_{B,n}/\mathrm{d}\phi$ is introduced, ensuring consistency with the prescribed damping rate. By solving (3.22), we can obtain an analytical expression for the wave amplitude of the oscillation in a three-layer fluid system according to potential flow theory (assuming counterclockwise). The corresponding expression for the interface fluctuation is given in (D1).

3.2. *The semi-analytical model*

The current modified model cannot satisfy the viscous boundary conditions at the interface and, therefore, cannot accurately capture the frequency shift. Bauer & Eidel (1999) and Ibrahim (2005) established a semi-analytical model for single-layer fluid that strictly satisfies sidewall boundary conditions, but is inconvenient to extend to multi-layer fluid systems. Kumar & Tuckerman (1994) and Batson *et al.* (2013) applied the Floquet series to the Faraday wave problem analytically in an infinite domain. The approach neglected viscous shear at the sidewall while keeping the strict interface boundary conditions and no-slip conditions at the top and bottom walls. This simplification is adequate for most regions far from the sidewall boundary layer. Experiments in cylindrical containers confirmed the validity of this theoretical approach (Batson *et al.* 2013; Ward *et al.* 2019*c*).

https://doi.org/10.1017/jfm.2025.10562 Published online by Cambridge University Press

Considering the $O(\varepsilon)$-order approximation, $\xi_A \approx h_1 + \eta_A$, $\xi_B \approx h_1 + h_2 + \eta_B$, the linear solutions can be expressed in the form of a Fourier series expansion

$$\bar{w}_j(r,\phi,z) = \sum_{n=1}^{\infty} W_{j,n}(z) J_1\left(k_{1,n} r\right) e^{i\phi}, \quad \bar{p}_j(r,\phi,z) = \sum_{n=1}^{\infty} P_{j,n}(z) J_1\left(k_{1,n} r\right) e^{i\phi},$$
$$\bar{\eta}_A(r,\phi) = \sum_{n=1}^{\infty} \zeta_{A,n} J_1\left(k_{1,n} r\right) e^{i\phi}, \quad \bar{\eta}_B(r,\phi) = \sum_{n=1}^{\infty} \zeta_{B,n} J_1\left(k_{1,n} r\right) e^{i\phi}, \tag{3.23}$$

with $\phi = \Omega t - \varphi$. In addition, $\bar{w}_j$ is the velocity in the z-direction and $\bar{p}_j$ is the pressure of fluid j in the form of complex functions. In addition, $\varepsilon_{1,n}$ represents the nth zero of the first-order Bessel function derivative $J_1'(\varepsilon_{1,n})$, $k_{1,n} = \varepsilon_{1,n}/R$, because the slip boundary on the side wall has been satisfied. Applying the divergence operator to the Navier–Stokes equations (3.2*b*) and simplifying, we obtain

$$\frac{\mathrm{d}^2 P_{j,n}}{\mathrm{d}z^2} - k_{1,n}^2 P_{j,n} = 0. \tag{3.24}$$

The general solution of the equation can be solved,

$$P_{j,n} = C_{j,n} e^{-k_{1,n} z} + D_{j,n} e^{k_{1,n} z^2}, \tag{3.25}$$

where $C_{j,n}$ and $D_{j,n}$ are undetermined coefficients.

Substituting the series solution (3.23) into (3.2*b*), we obtain

$$\frac{\mathrm{d}^2 W_{j,n}}{\mathrm{d}z^2} - \left(k_{1,n}^2 + \frac{\mathrm{i}\Omega}{v_j}\right) W_{j,n} = \frac{1}{\mu_j} \frac{\mathrm{d}P_{j,n}}{\mathrm{d}z}. \tag{3.26}$$

Solving (3.26), we obtain the general solution for $W_{j,n}$,

$$W_{j,n} = A_{j,n} \mathrm{e}^{-\sqrt{k_{1,n}^2 + \mathrm{i}\frac{\Omega}{v_j}}\, z} + B_{j,n} \mathrm{e}^{\sqrt{k_{1,n}^2 + \mathrm{i}\frac{\Omega}{v_j}}\, z} + C_{j,n} \frac{-\mathrm{i}k_{1,n}}{\rho_j \Omega} \mathrm{e}^{-k_{1,n} z} + D_{j,n} \frac{\mathrm{i}k_{1,n}}{\rho_j \Omega} \mathrm{e}^{k_{1,n} z}, \tag{3.27}$$

where $A_{j,n}$ and $B_{j,n}$ are undetermined coefficients.

The boundary conditions are also expressed as follows.

(i) Velocity boundary conditions:

$$W_{1,n}\big|_{z=0} = 0, \ \left.\frac{\mathrm{d}W_{1,n}}{\mathrm{d}z}\right|_{z=0} = 0,$$
$$W_{1,n}\big|_{z=h_1} = W_{2,n}\big|_{z=h_1} = \mathrm{i}\Omega\zeta_{A,n}, \ \left.\frac{\mathrm{d}W_{1,n}}{\mathrm{d}z}\right|_{z=h_1} = \left.\frac{\mathrm{d}W_{2,n}}{\mathrm{d}z}\right|_{z=h_1},$$
$$W_{1,n}\big|_{z=h_1+h_2} = W_{2,n}\big|_{z=h_1+h_2} = \mathrm{i}\Omega\zeta_{B,l}, \ \left.\frac{\mathrm{d}W_{1,n}}{\mathrm{d}z}\right|_{z=h_1+h_2} = \left.\frac{\mathrm{d}W_{2,n}}{\mathrm{d}z}\right|_{z=h_1+h_2},$$
$$W_{3,n}\big|_{z=\sum h_i} = 0, \ \left.\frac{\mathrm{d}W_{3,n}}{\mathrm{d}z}\right|_{z=\sum h_i} = 0. \tag{3.28}$$

https://doi.org/10.1017/jfm.2025.10562 Published online by Cambridge University Press

(ii) Shear stress boundary conditions:

$$\mu_1\left(k_{1,n}^2W_{1,n}+\frac{\mathrm{d}^2W_{1,n}}{\mathrm{d}z^2}\right)\bigg|_{z=h_1}-\mu_2\left(k_{1,n}^2W_{2,n}+\frac{\mathrm{d}^2W_{2,n}}{\mathrm{d}z^2}\right)\bigg|_{z=h_1}=0,$$

$$\mu_2\left(k_{1,n}^2W_{2,n}+\frac{\mathrm{d}^2W_{2,n}}{\mathrm{d}z^2}\right)\bigg|_{z=h_1+h_2}-\mu_3\left(k_{1,n}^2W_{3,n}+\frac{\mathrm{d}^2W_{3,n}}{\mathrm{d}z^2}\right)\bigg|_{z=h_1+h_2}=0. \tag{3.29}$$

(iii) Normal stress boundary conditions:

$$\begin{aligned}
&P_{1,n}\big|_{z=h_1}-P_{2,n}\big|_{z=h_1}-2\left(\mu_1-\mu_2\right)\frac{\mathrm{d}W_{1,n}}{\mathrm{d}z}\bigg|_{z=h_1}\\
&-\left[(\rho_1-\rho_2)g+\sigma_Ak_{1,n}^2\right]\zeta_{A,n}=-\frac{R\left(\rho_1-\rho_2\right)d_s\Omega^2}{\left(k_{1,n}^2R^2-1\right)J_1\left(k_{1,n}R\right)}\\
&P_{2,n}\big|_{z=h_1+h_2}-P_{3,n}\big|_{z=h_1+h_2}-2\left(\mu_2-\mu_3\right)\frac{\mathrm{d}W_{3,n}}{\mathrm{d}z}\bigg|_{z=h_1+h_2}\\
&-\left[(\rho_2-\rho_3)g+\sigma_Bk_{1,n}^2\right]\zeta_{B,l}=-\frac{R\left(\rho_2-\rho_3\right)d_s\Omega^2}{\left(k_{1,n}^2R^2-1\right)J_1\left(k_{1,n}R\right)}.
\end{aligned} \tag{3.30}$$

Substituting (3.25), (3.27) into (3.28), (3.29), (3.30) allows us to solve for $A_{j,n}$, $B_{j,n}$, $C_{j,n}$, $D_{j,n}$, $\zeta_{A,n}$ and $\zeta_{B,n}$, where $j=1,2,3$. The boundary conditions (3.28), (3.29), (3.30) provide 14 equations, allowing the determination of 14 unknowns for any given positive integer n. The counterclockwise solutions of η_A and η_B are the real solution,

$$\begin{aligned}
\eta_A &= \delta_A\cos\left(\phi+\varphi_A\right)=\mathrm{Re}\left(\bar{\eta}_A\right)\\
&= \left(\mathrm{Re}\left(\sum_{n=1}^{\infty}\zeta_{A,n}J_1\left(k_{1,n}r\right)\right)\cos\phi-\mathrm{Im}\left(\sum_{n=1}^{\infty}\zeta_{A,n}J_1\left(k_{1,n}r\right)\right)\sin\phi\right),\\
\eta_B &= \delta_B\cos\left(\phi+\varphi_B\right)=\mathrm{Re}\left(\bar{\eta}_B\right)\\
&= \left(\mathrm{Re}\left(\sum_{n=1}^{\infty}\zeta_{B,n}J_1\left(k_{1,n}r\right)\right)\cos\phi-\mathrm{Im}\left(\sum_{n=1}^{\infty}\zeta_{B,n}J_1\left(k_{1,n}r\right)\right)\sin\phi\right),
\end{aligned} \tag{3.31}$$

with

$$\begin{aligned}
&\delta_A(r)=\left|\sum_{n=1}^{\infty}\zeta_{A,n}J_1\left(k_{1,n}r\right)\right|,\ \delta_B(r)=\left|\sum_{n=1}^{\infty}\zeta_{B,n}J_1\left(k_{1,n}r\right)\right|,\\
&\varphi_A=\arctan\frac{\mathrm{Im}\left(\sum_{n=1}^{\infty}\zeta_{A,n}J_1\left(k_{1,n}r\right)\right)}{\mathrm{Re}\left(\sum_{n=1}^{\infty}\zeta_{A,n}J_1\left(k_{1,n}r\right)\right)},\ \varphi_B=\arctan\frac{\mathrm{Im}\left(\sum_{n=1}^{\infty}\zeta_{B,n}J_1\left(k_{1,n}r\right)\right)}{\mathrm{Re}\left(\sum_{n=1}^{\infty}\zeta_{B,n}J_1\left(k_{1,n}r\right)\right)}.
\end{aligned} \tag{3.32}$$

4. Scaling laws

We define the Froude number $Fr=d_s\Omega^2/(2g)$, which represents the ratio of inertial force to gravitational force, and Reynold number $Re_j=\Omega R^2/\nu_j$, which represents the ratio of inertial force to viscous force. With the Air|P|S system as a reference, we calculate the variation of the amplitude ratio δ_A/δ_B and phase difference $\varphi/2\pi$ with Fr for different

https://doi.org/10.1017/jfm.2025.10562 Published online by Cambridge University Press

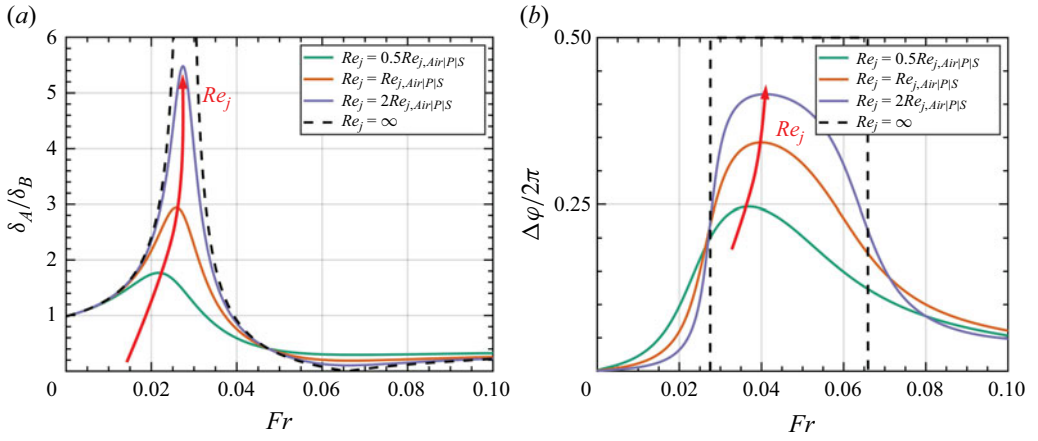


Figure 3. Variation of amplitude ratio and phase difference with Fr for different Reynolds numbers. Here, $Re_{j,Air|P|S}$ represents the Reynolds number of the jth fluid layer in the Air|P|S fluid system. At $Fr = 0.01$, the Reynolds numbers for the three fluid layers are $Re_1 = 90$, $Re_2 = 112$ and $Re_3 = 303$. When $Fr = 0.1$, they increase to $Re_1 = 283$, $Re_2 = 354$ and $Re_3 = 957$, respectively, indicating that $Re_i \gg 1$ in all cases. Other parameters are the same as those of Air|P|S.

Re_j. As shown in figure 3, the amplitude ratio and phase difference reach their maximum values at resonance from the calculations of § 3.2. At resonance, the amplitude ratio δ_A/δ_B and the phase difference $\varphi/2\pi$ increase with increasing Re_j. When $Re_j = \infty$, the wave amplitude ratio exhibits non-physical singularities and the phase difference undergoes an abrupt shift at resonance. However, the viscous model eliminates these singularities in amplitude and discontinuities in phase difference, providing a more realistic description of near resonance.

While the semi-analytical model offers higher accuracy by fully resolving viscous effects, its analytical complexity limits its utility for scaling analysis. The modified model, however, enables a convenient perturbative approach, making it well suited for extracting the scaling behaviours of the system. We separately decompose $\beta_{A,n}$ and $\beta_{B,n}$ into components $\beta_{A,n} = \beta_{A,S,n}\sin\phi + \beta_{A,C,n}\cos\phi$ and $\beta_{B,n} = \beta_{B,S,n}\sin\phi + \beta_{B,C,n}\cos\phi$. However, we consider the characteristics of solutions far from resonance. The small perturbation expansion of (D1) is conducted with $\Upsilon = \lambda/\Omega \ll 1$. From (D5), which is a non-resonant asymptotic solution, we know $\beta_{A,C,n}$, $\beta_{B,C,n} \sim \Upsilon$. Therefore, η_A, $\eta_B \sim \Upsilon$ far from resonance. However, we apply the small perturbation expansion at resonance satisfying $\gamma_n = 0$. From (D6), which is the non-resonant asymptotic solution, we know $\beta_{A,C,n}$, $\beta_{B,C,n} \sim \Upsilon^{-1}$. Therefore, η_A, $\eta_B \sim \Upsilon^{-1}$ at resonance.

At resonance, when $|\tan\varphi_A| \ll 1$ and $|\tan\varphi_B| \ll 1$, the phase difference reaches an extremum φ_{max}, which approximately satisfies

$$\pi - \Delta\varphi_{max} \approx \frac{\beta_{A,S,n}}{\beta_{A,C,n}} - \frac{\beta_{B,S,n}}{\beta_{B,C,n}}, \tag{4.1}$$

because $\Delta\varphi_{max}$ is close to π, such that $\Delta\varphi_{max} \approx \tan\Delta\varphi_{max} \approx \tan\varphi_B - \tan\varphi_A$. Moreover, since the resonant wave amplitudes scale as η_A, $\eta_B \sim \Upsilon^{-1}$, the resulting phase difference follows the scaling law $\pi - \Delta\varphi_{max} \sim \Upsilon$.

Using the semi-analytical model in § 3.2, we compute δ_A and $\Delta\phi$ over the range $Fr = 0 \sim 0.1$, from which the first-order resonance peak values $\delta_{A,max}$ and $\Delta\phi_{max}$ are extracted. Figure 4 displays the relationships between the first-order resonant amplitude $\delta_{A,max}$ of interface A, the maximum phase difference $\Delta\varphi_{max}$, and the viscous damping

https://doi.org/10.1017/jfm.2025.10562 Published online by Cambridge University Press

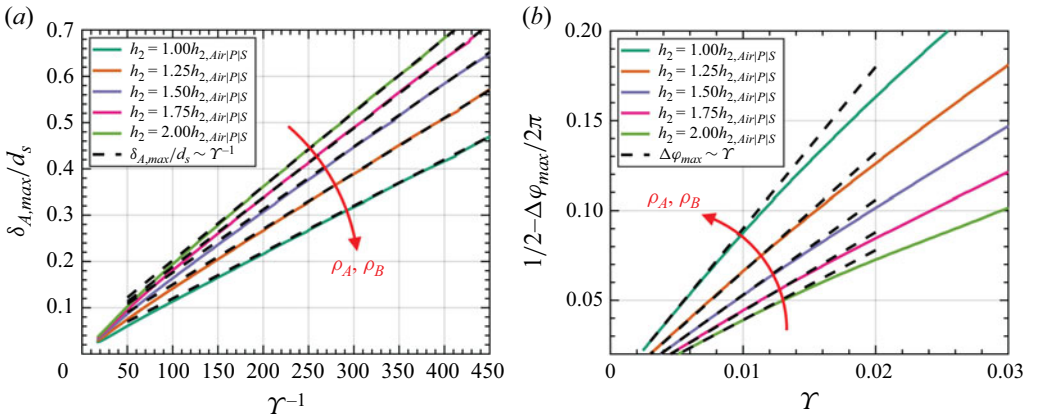


Figure 4. Normalised resonance amplitude and phase difference maximum. (*a*) Dimensionless resonance amplitude at interface A as a function of Υ^{-1}. The red arrows indicate the direction of enhanced coupling. (*b*) Maximum of phase difference $\Delta\varphi_{max}$ as a function of Υ. The viscosity $Re_j = \Omega R^2/\nu_j$ ranges from 0.01 to 10 times the original fluid viscosity of Air|P|S. Here, $Re_{j,Air|P|S}$ represents the Reynolds number of the jth fluid layer in the Air|P|S fluid system. Other parameters are the same as those of Air|P|S.

Υ of the fluid system. In figure 4(*a*), the first-order resonant amplitude of interface A increases with the rise of Υ^{-1}, indicating that higher viscous damping in the fluid system leads to smaller resonant amplitude. When the fluid system exhibits low viscous damping $\Upsilon^{-1} \gg 1$, the first-order resonant amplitude satisfies $\delta_{A,max}/\mathrm{d}s \sim \Upsilon^{-1}$, as the condition $\eta_A, \eta_B \sim \Upsilon^{-1}$ is satisfied at resonance. This conclusion is consistent with Horstmann *et al.* (2021), namely $\delta_{max}/R \sim \sqrt{Re_j}$, because $\lambda \sim Re_j^{-1/2}$. The maximum phase difference between interface A and interface B approaches π as Υ decreases. Under low viscous damping conditions ($\Upsilon \ll 1$), the maximum phase difference satisfies $\pi - \Delta\varphi_{max} \sim \Upsilon$, as illustrated in figure 4(*b*). Additionally, as the coupling coefficients $\rho_{A,n}$ and $\rho_{B,n}$ increase, the maximum amplitude of interface A decreases, and the maximum phase difference also decreases. This behaviour is related to energy transfer between interfaces A and B.

Therefore, we further explore the changes in kinetic energy caused by interface coupling, using $\tilde{\boldsymbol{u}}_B^2 = \boldsymbol{u}_B^2/(d_s\Omega)^2$ to quantify the interfacial kinetic energy at interface B, where $\tilde{\boldsymbol{u}}_B$ represents the interfacial normalised velocity. Furthermore, dimensional analysis suggests that the interfacial velocity $\boldsymbol{u_B}^2$ satisfies the scaling relation $|\boldsymbol{u}_B| \sim \Omega\eta_B$. Therefore, $\boldsymbol{u_B}^2$ satisfies $\boldsymbol{u}_B^2 \sim \eta_B^2 \sim \Upsilon^{-2}$ following the resonance condition. Compared with the two-layer fluid system (Air|P), introducing an additional fluid interface in the three-layer configuration (Air|P|S) significantly changes the interfacial dynamics. This additional P–S interface is a conduit for enhanced energy exchange between layers. As illustrated in figure 5(*a*), the presence of the intermediate silicone oil (S) layer leads to a pronounced jump in kinetic energy at interface B (Air–Paraffin oil interface) when the system is driven at the resonant frequency $\Omega = \Omega_A$, corresponding to the natural frequency of the Air|P configuration. This abrupt increase is reminiscent of the classic dead water phenomenon first described by Ekman (1904) in his doctoral thesis, wherein a vessel moving through a stratified fluid experiences a significantly greater drag than in an homogeneous fluid (Mercier, Vasseur & Dauxois 2011). The enhanced resistance arises from wave generation at the fluid interface, which extracts energy from the moving body. The effect is most pronounced when the vessel speed is below the maximum phase speed of interfacial waves, with the interfacial kinetic energy $\boldsymbol{u}^2$ as a proxy for the drag (Fourdrinoy *et al.*

https://doi.org/10.1017/jfm.2025.10562 Published online by Cambridge University Press

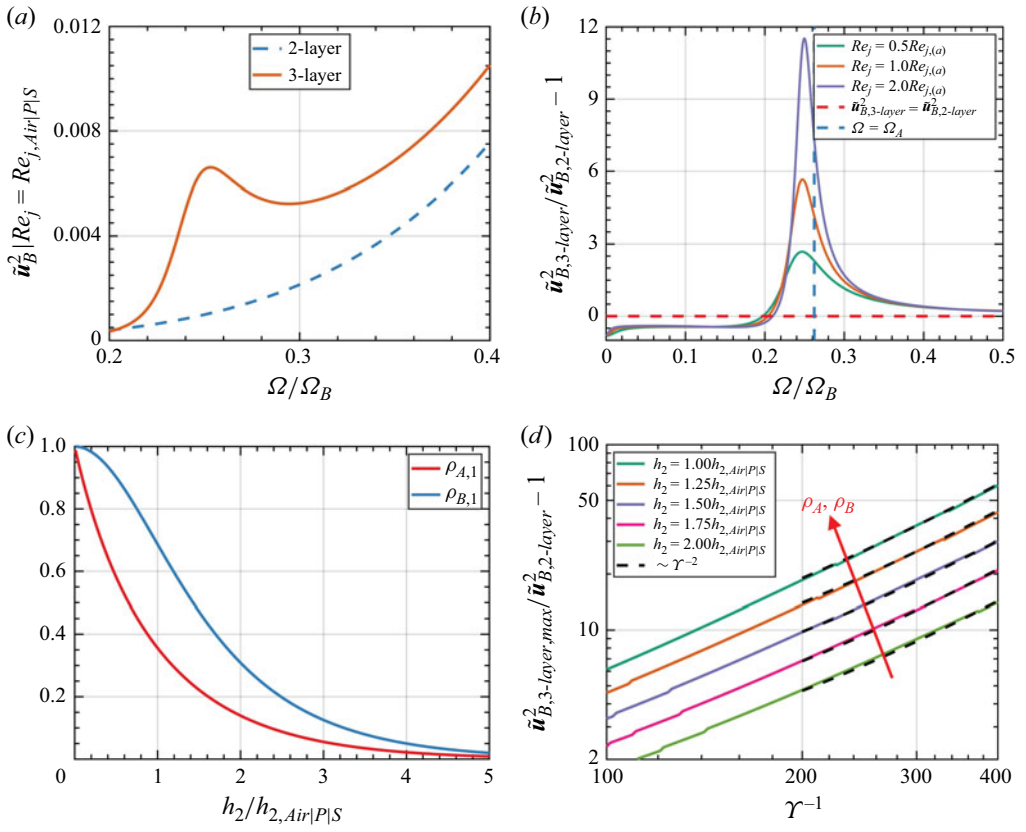


Figure 5. Impact of additional fluid layers on interfacial kinetic energy. (*a*) Comparison of interfacial kinetic energy as a function of frequency in a three-layer fluid system (Air|P|S system) and a two-layer fluid system (Air|P system) with 50 cst of silicone oil and $h_2 = 20$ mm. (*b*) Relationship between the kinetic energy growth rate and frequency for different Reynolds numbers Re_j. (*c*) Coupling parameters ρ_A, ρ_B as a function of $h_2/h_{2,Air|P|S}$. (*d*) Relationship between the maximum kinetic energy growth rate and Υ^{-1}. $Re_{j,Air|P|S}$ represents the Reynolds number of the jth fluid layer in the Air|P|S fluid system. Other parameters are the same as those of Air|P|S.

2020). Figure 5(*b*) reveals that this kinetic energy jump becomes more abrupt as viscosity decreases, indicating that viscous shear plays a mitigating role. In the low-viscosity limit ($\Upsilon^{-1} \gg 1$), the energy growth rate follows $\tilde{\boldsymbol{u}}^2_{B,3-layer,max}/\tilde{\boldsymbol{u}}^2_{B,2-layer} \sim \Upsilon^{-2}$, consistent with $\boldsymbol{u}_B^2 \sim \Upsilon^{-2}$. Moreover, as shown in figure 5(*c, d*), stronger interfacial coupling amplifies this resonant energy growth, particularly when the intermediate fluid layer is thin. Introducing a third, thin interfacial layer substantially increases energy transfer and drag by exciting interfacial waves at multiple boundaries. This enhanced coupling effectively mimics the sharp density transition in classical two-layer systems, reinforcing the analogy to Ekman's dead water.

Through calculations using the theoretical model, we observed BOS patterns with spiral structures similar to those found in experiments on two-layer fluid systems (Horstmann *et al.* 2021), as shown in figure 6. The number of spiral arms increases with the sloshing frequency. Additionally, as the viscosity of the bottom fluid layer increases, the system gradually transitions from underdamped to overdamped characteristics.

https://doi.org/10.1017/jfm.2025.10562 Published online by Cambridge University Press

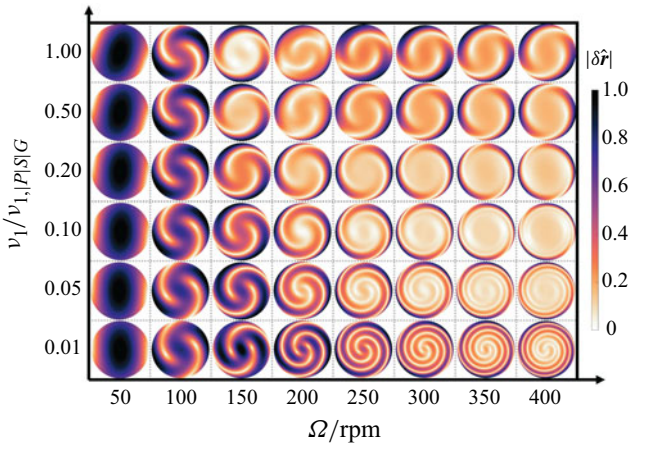


Figure 6. BOS images corresponding to the different viscosity of fluid 1 and shaking frequency, where $\nu_{1,P|S|G}$ is the kinematic viscosity of glycerol. Other parameters are the same as those of P|S|G.

5. Comparison with experimental data

To measure the amplitude and phase quantitatively of the interfaces, we use ultrasonic techniques previously introduced by Horstmann *et al.* (2019) to measure the wave amplitudes of a single fluid interface. This approach enables the simultaneous measurement of fluctuations in the two fluid interfaces. For ultrasonic measurement technology, we use the Air|P|S fluid system to avoid extreme damping of ultrasonic waves in the fluid. In figures 7(*a*)–7(*c*) and figures 8(*a*)–8(*c*), the kinematic viscosity of silicone oil is 50 cst. In figures 7(*d*)–7(*f*) and figures 8(*d*)–8(*f*), the kinematic viscosity of silicone oil is 500 cst. Additionally, the initial thickness of the paraffin oil layer is 20 mm in figures 7(*a, d*) and 8(*a, d*), 25 mm in figures 7(*b, e*) and 8(*b, e*), and 30 mm in figures 7 (*c, f*) and 8(*c, f*). The ultrasonic probe is fixed at $r_0 = 30$ mm.

We perform a comparative evaluation of the model predictions against experimental data for the three-layer fluid system, as plotted in figures 7 and 8. The amplitudes at $r = r_0$ on both interfaces are measured using ultrasonic techniques, as indicated in figure 7 by the hollow circles. The results calculated using the semi-analytical and modified models agree well with the experimental data. Similar to the two-layer fluid system, the semi-analytical model captures more accurately the frequency shift caused by viscosity. It confirms that the primary boundary conditions are associated with the interface in the flow field near the interface and away from the sidewall boundary layer. The influence of the convection and other higher-order terms drives the deviation from experimental measurements and the two models. On the one hand, the premise of the model in this article is based on the linear wave assumption; therefore, when the amplitude is large, there may be some deviation from the experiments. On the other hand, the amplitude of resonance may lead to a smaller amplitude than linear waves due to superharmonic resonance (Bongarzone *et al.* 2022). Due to viscosity, phase differences, φ_A and φ_B, exist between the two interfaces and the shaker, as illustrated in figure 1(*b*). As shown in figure 8, $\Delta\varphi = \varphi_B - \varphi_A$ is well captured by ultrasound techniques. Both the semi-analytical model and the modified model can capture the phase difference. However, the results of the semi-analytical model are closer to the experimental values, attributed to fully satisfying the fluid dynamics equations and interface boundary conditions. Figure 8 shows that interface A primarily contributes to the phase difference between the two interfaces. Passing the first resonance point, interface A introduces a phase shift close to $\pi/2$ (exactly $\pi/2$ in the inviscid case) relative to the

https://doi.org/10.1017/jfm.2025.10562 Published online by Cambridge University Press

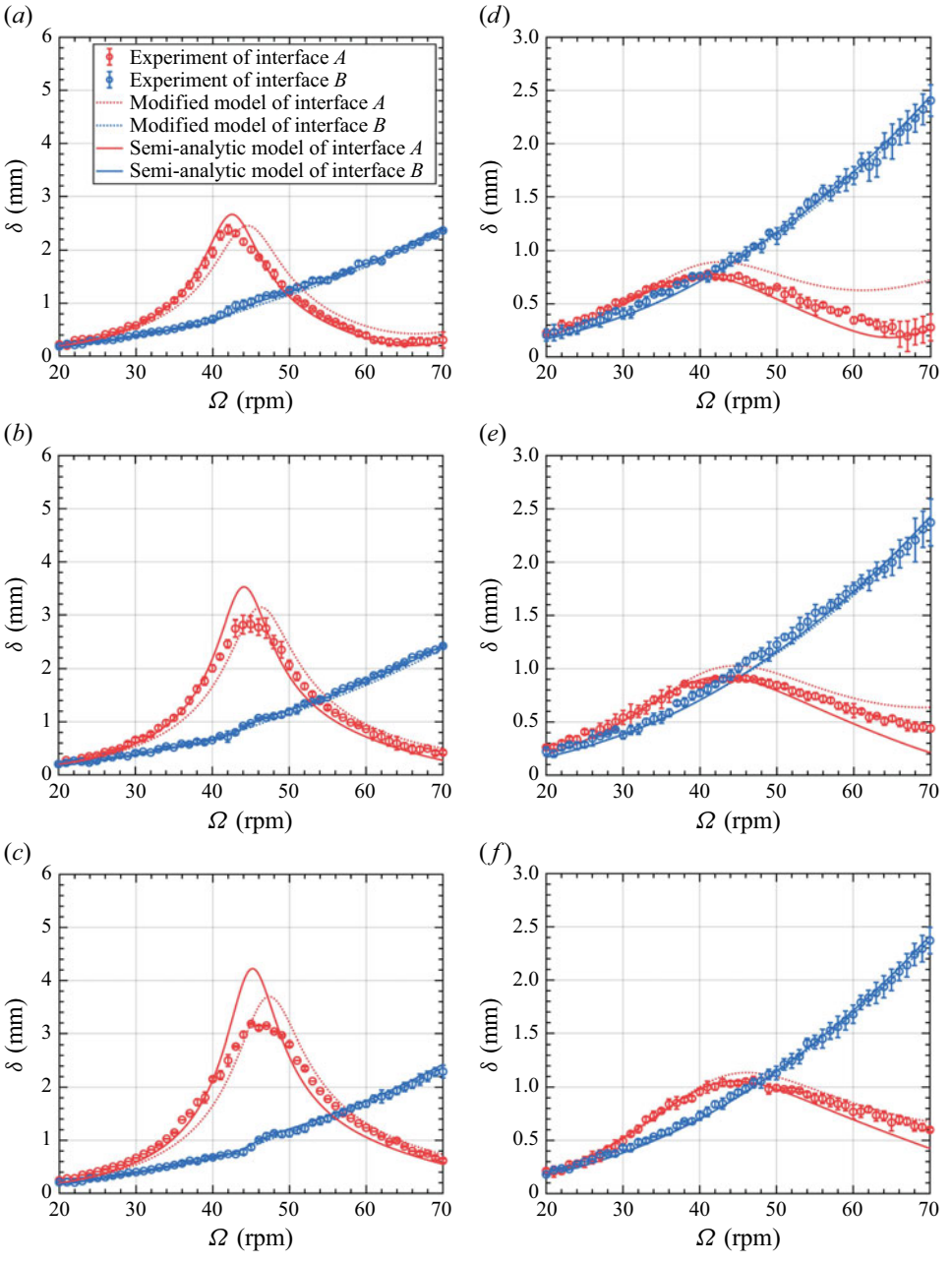


Figure 7. Comparison of experimental measurements and theoretical predictions of the wave amplitudes, δ_A and δ_B, in the three-layer fluid system. We select three typical thicknesses of middle-layer paraffin oil, (*a, d*) 20 mm, (*b, e*) 25 mm and (*c ,f*) 30 mm. The viscosity of silicone oil is 50 cst in figures 7(*a*)–7(*c*) and 500 cst in figures 7(*d*)–7(*f*). The hollow circles denote experimental data, the dashed lines show the data predicted by the modified model and the solid lines represent the predictions calculated by the semi-analytic model.

sloshing platform, while interface *B* remains far from its resonance point. To highlight the advantage of the semi-analytical model in capturing the viscous frequency shift, figure 9 compares its predictions, those of the modified model and experimental measurements. The semi-analytical results show significantly better agreement with the experimental data.

https://doi.org/10.1017/jfm.2025.10562 Published online by Cambridge University Press

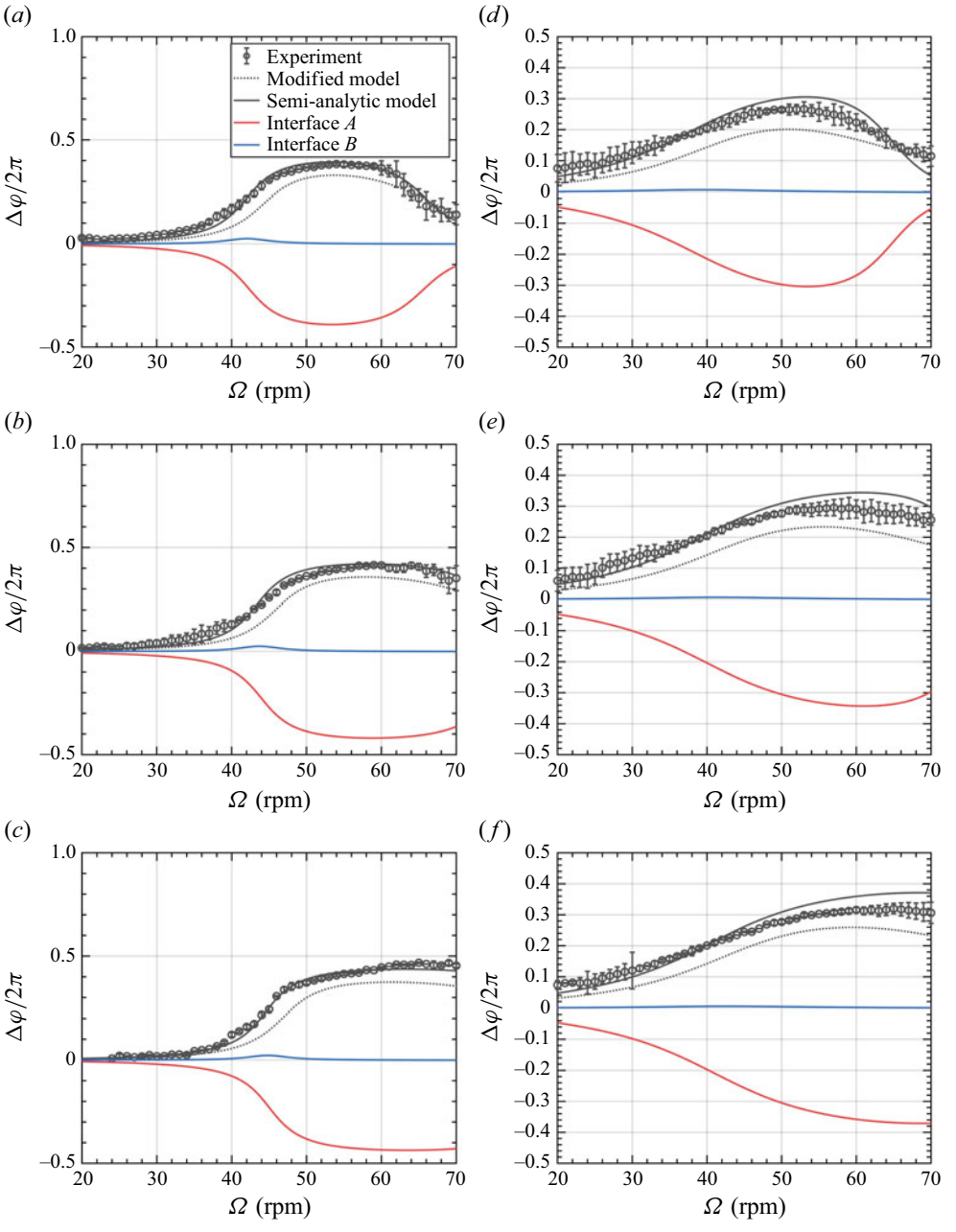


Figure 8. Comparison of experimental measurements and theoretical predictions of the phase difference $\Delta\varphi$ of interface waves in the three-layer fluid system. We select three typical thicknesses of middle-layer paraffin oil, (*a, d*) 20 mm, (*b, e*) 25 mm and (*c, f*) 30 mm. The viscosity of silicone oil is 50 cst in figures 8(*a*)–8(*c*) and 500 cst in figures 8(*d*)–8(*f*). φ_A and φ_B represent the phase differences between interfaces and the shaker. The red (φ_A) and blue (φ_B) dashed lines in the graph represent the phase differences between interfaces and the shaker, as calculated by the semi-analytical model.

https://doi.org/10.1017/jfm.2025.10562 Published online by Cambridge University Press

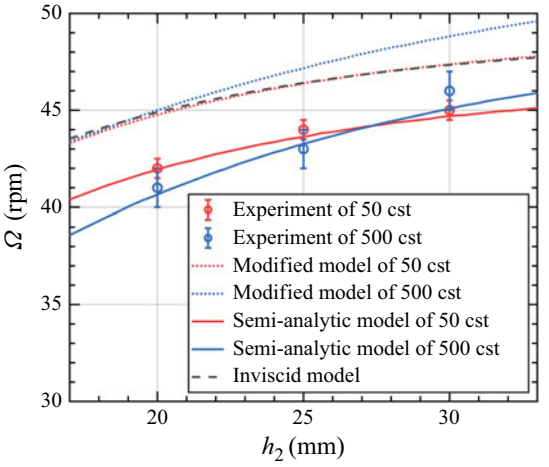


Figure 9. Comparison of experimental measurements and theoretical predictions of the resonance frequency of interface A.

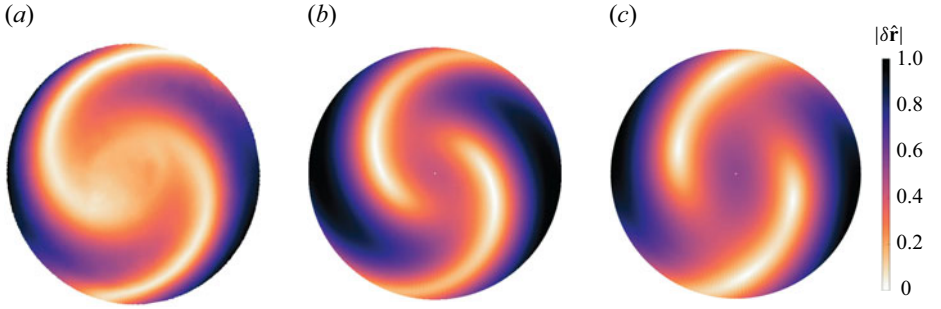


Figure 10. Normalisation of the sum of gradients of internal waves at two interfaces. (a) Experimental results were obtained by using the BOS method with $\Omega = 100$ rpm. (b) Reconstructed results from the semi-analytical model with $\Omega = 100$ rpm. (c) Reconstructed results from the modified model with $\Omega = 100$ rpm.

By numerically solving the semi-analytical model and the modified model, the spiral arm patterns are observed in the three-layer fluid system, as shown in figure 6. To validate this theoretical finding, we applied the BOS technique to capture wave gradient information in a two-dimensional plane for the P|S|G fluid system. The results in figure 10 show that both the semi-analytical and modified models provide reliable predictions not only for the wave height, but also for the estimation of the interface except near the sidewalls from figure 10. We experimentally measure the gradient distribution of the interface except near the sidewalls. Using the BOS technique, we experimentally measured the gradient distribution of interface waves, as shown in figure 10(a). Our measured data validate the spiral arm structure predicted by both the semi-analytical model (figure 10b) and the modified model (figure 10c). Moreover, the results of the semi-analytic model are more consistent with the measured results, as evident in the angle of the spiral arm caused by the viscosity. The discrepancy can be attributed to the effects of BOS and the normalisation process. Specifically, local defects in the container or the speckle paper may result in excessive local measurement gradients due to the BOS, which impacts

https://doi.org/10.1017/jfm.2025.10562 Published online by Cambridge University Press

the alignment between the normalised values and the theoretical predictions. However, it is important to note that this issue does not compromise the overall validity of the comparative analysis.

Both theoretical models presented in this study rely on the assumption of linear waves, i.e. the wave amplitude is much smaller than the wave height and wavelength. The modified model, which introduces a viscous damping term into the inviscid solution, is valid under the condition $Re_j \gg 1$. The non-dimensional parameter Υ can quantify this requirement more precisely, with $\Upsilon \ll 1$ equivalent to $Re_j \gg 1$. Figure 4 of the manuscript shows that the modified model remains accurate when $\Upsilon < 0.01$. In contrast, the semi-analytical model does not rely on the assumption $Re_j \gg 1$, as it directly solves the linearised Navier–Stokes equations with viscous terms retained. However, this model is constrained by the boundary conditions at the lateral wall. Since the solution is constructed using a Fourier series expansion in an azimuthally unbounded domain, it effectively captures the dynamics in the central region far from the container sidewall. This is also why ultrasonic probes measure the interfacial amplitude away from the boundary layer instead of tracking the contact line. Additional boundary conditions must be imposed on both models if a pinned contact line is present. In such cases, it is often necessary to solve an integro-differential system, as shown by Shao *et al.* (2021). Moreover, both models are first-order approximations, neglecting mean drift velocities arising from nonlinear convective terms (Bongarzone & Gallaire 2024). Capturing such effects would require extending the expansion to the second order. At least third-order approximations may be necessary for pronounced superharmonic responses with multiple wave crests (Bongarzone *et al.* 2022).

6. Conclusion

In this paper, we establish a sloshing platform to generate sloshing waves in a three-layer viscous fluid system and employ ultrasonic technology to measure the interface positions. Additionally, the BOS technique is extended to the three-layer fluid system, successfully capturing spiral interface patterns. According to the Horstmann model, we derive a new model including viscous coupling terms that enable us to understand the kinetic energy transfer between two interfaces in a three-layer fluid system.

Furthermore, we obtain a semi-analytical solution from the Fourier-expanded form of the Navier–Stokes equations which give a nearly exact prediction of the wave amplitude and phase. The semi-analytical model fully satisfies the interfaces' kinematic and dynamic boundary conditions at the interface, enabling it to capture better the phase difference and frequency shift phenomena caused by viscous shear. The semi-analytical model is found to explain the experimental data better than the modified model.

In addition, we have examined the effects of Fr, Re_j and the coupling coefficients (ρ_A, ρ_B) on the interfacial amplitude and phase. We find that in low-viscosity fluid systems, the first-order resonant amplitude follows the relation $\delta_{A,max}/\mathrm{d}s \sim \Upsilon^{-1}$ and the maximum phase difference satisfies $\pi - \Delta\varphi_{max} \sim \Upsilon$, which is valuable for understanding the dead water phenomenon. The addition of fluid layers leads to new resonances and abrupt increases in interfacial kinetic energy, with the growth rate relative to the two-layer fluid system satisfying $\tilde{\boldsymbol{u}}^2_{B,3\text{-}layer,max}/\tilde{\boldsymbol{u}}^2_{B,2\text{-}layer} \sim \Upsilon^{-2}$.

In future work, we intend to extend our theoretical model to continuous density gradient fluid systems to explore energy transfer in detail. Moreover, extension of the semi-analytical model to multiphysics systems will be important for advancing the understanding of MPR waves (Horstmann *et al.* 2018; Herreman *et al.* 2023).

https://doi.org/10.1017/jfm.2025.10562 Published online by Cambridge University Press

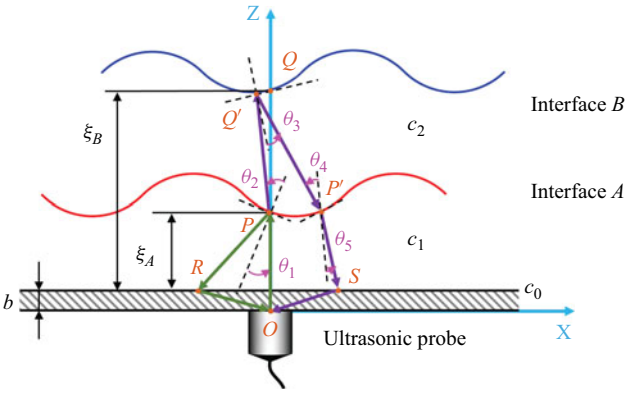


Figure 11. Schematic diagram of the acoustic path for ultrasonic measurement of liquid thickness.

Acknowledgements. The authors greatly appreciate the anonymous reviewers for their comments, which significantly improved the manuscript.

Funding. The authors gratefully acknowledge support from NSFC (#52222607, #52176086, #12102333, #51927812), and National Key Research and Development Program of China (#2022YFE03130000).

Declaration of interests. The authors report no conflict of interest.

Appendix A. Ultrasonic measurement

For simplicity in derivation, we consider ultrasonic longitudinal waves within the (x, z) plane, as shown in figure 11, satisfying the law of reflection and the law of refraction. According to the geometric relationships, we know that the shortest time for the probe to transmit and receive the ultrasound wave reflected from interface A is $t_A = (b + L_{RO})/c_0 + (\xi_A + L_{PR})/c_1$. Similarly, the corresponding time for the ultrasound reflected from interface B is $t_B = (b + L_{SO})/c_0 + (\xi_A + L_{P'S})/c_1 + (L_{PO'} + L_{O'P'})/c_2$, where c_0, c_1 and c_2 are the sound speeds of acrylic, fluid 1 and fluid 2, respectively.

Using geometric relationships, the first-order Taylor expansion and the law of reflection, we know

$$\begin{aligned} z_{Q'} &= \xi_B - \left.\frac{\partial \xi_B}{\partial x}\right|_{x=0} (\xi_B - \xi_A)\tan(\theta_2 - \theta_1), \\ z_{P'} &= z_{Q'} - L_{Q'P'}\cos(-\theta_1 + \theta_2 + 2\theta_3), \\ x_S &= y_{P'}\tan(-\theta_1 + \theta_2 + 2\theta_3 - \theta_4 + \theta_5), \end{aligned} \tag{A1}$$

$$\theta_4 = 2\theta_3 + \theta_2 - \theta_1 - \alpha, \quad \tan\alpha = \left.\frac{\partial \xi_A}{\partial x}\right|_{x=0},$$

$$\theta_3 = \left.\frac{\partial \xi_B}{\partial x}\right|_{x=0} - (\theta_2 - \theta_1), \quad \tan\theta_1 = \left.\frac{\partial \xi_A}{\partial x}\right|_{x=0}, \tag{A2}$$

$$L_{PR} = \frac{\xi_A}{\cos 2\theta_1}, \quad L_{RO} = \sqrt{(\xi_A \tan 2\theta_1)^2 + b^2},$$

$$L_{PQ'} = \frac{\xi_B - \xi_A}{\cos(\theta_2 - \theta_1)}, \quad L_{Q'P'} = \frac{L_{PQ'}\cos(-\theta_1 + \theta_2 - \alpha)}{\cos(-\theta_1 + \theta_2 + 2\theta_3 - \alpha)},$$

$$L_{P'S} = \frac{y_{P'}}{\cos(-\theta_1 + \theta_2 + 2\theta_3 - \theta_4 + \theta_5)}, \quad L_{SO} = \sqrt{x_S^2 + b^2}. \tag{A3}$$

https://doi.org/10.1017/jfm.2025.10562 Published online by Cambridge University Press

According to the law of refraction, we know

$$\frac{\sin\theta_1}{c_1}=\frac{\sin\theta_2}{c_2},\ \frac{\sin\theta_5}{c_1}=\frac{\sin\theta_4}{c_2}. \tag{A4}$$

Next, considering the small amplitude assumption used in this paper, we have the following order of magnitude relationships:

$$\begin{aligned}
&\varepsilon=\max\left\{\left|\xi_A-h_1\right|,\quad \left|\xi_B-(h_1+h_2)\right|\right\}/\lambda_w\ll 1,\\
&\quad\left|\xi_A-h_1\right|/h_1=O(\varepsilon),\\
&\left|\xi_B-(h_1+h_2)\right|/(h_1+h_2)=O(\varepsilon),\\
&\quad\theta_1,\theta_2,\theta_3,\theta_4,\theta_5=O(\varepsilon),\\
&\quad\left.\frac{\partial\xi_A}{\partial x}\right|_{x=0}=O(\varepsilon),\ \left.\frac{\partial\xi_B}{\partial x}\right|_{x=0}=O(\varepsilon),
\end{aligned} \tag{A5}$$

where λ_w is the wavelength. Therefore, we can perform a small perturbation expansion for t_A and t_B,

$$\begin{aligned}
t_A=&\frac{2\xi_A}{c_1}+\frac{2b}{c_0}+2h_1\left(\frac{1}{c_1}+\frac{h_1}{bc_0}\right)\left(\left.\frac{\partial\xi_A}{\partial x}\right|_{x=0}\right)^2+O\left(\varepsilon^3\right),\\
t_B=&\frac{2b}{c_0}+\frac{2\xi_A}{c_1}+\frac{2\left(\xi_B-\xi_A\right)}{c_2}\\
&+\frac{1}{2}\frac{h_1}{bc_0}\left(\left(\frac{c_2}{c_1}-1\right)\left(\frac{c_2}{c_1}-3\right)\left.\frac{\partial\xi_A}{\partial x}\right|_{x=0}+2\frac{c_1}{c_2}\left.\frac{\partial\xi_B}{\partial x}\right|_{x=0}\right)^2\frac{h_1}{c_0}\\
&+2\left(2-\frac{c_2}{c_1}-\frac{c_1}{c_2}\right)^2\left(\left.\frac{\partial\xi_A}{\partial x}\right|_{x=0}\right)^2\frac{h_1}{c_1}\\
&+4\left(2-\frac{c_2}{c_1}-\frac{c_1}{c_2}\right)\left(\frac{c_1}{c_2}\right)\left.\frac{\partial\xi_A}{\partial x}\right|_{x=0}\left.\frac{\partial\xi_B}{\partial x}\right|_{x=0}\frac{h_1}{c_1}+2\left(\frac{c_1}{c_2}\right)^2\left(\left.\frac{\partial\xi_B}{\partial x}\right|_{x=0}\right)^2\frac{h_1}{c_1}\\
&+2\left(\left(\frac{c_2}{c_1}-1+\left(2-\frac{c_2}{c_1}-\frac{c_1}{c_2}\right)^2\right)\left(\left.\frac{\partial\xi_A}{\partial x}\right|_{x=0}\right)^2+\left(2+\left(\frac{c_1}{c_2}\right)^2\right)\left(\left.\frac{\partial\xi_B}{\partial x}\right|_{x=0}\right)^2\right)\frac{h_2}{c_1}\\
&+2\left(\frac{1}{2}\left(\frac{c_2}{c_1}-1\right)+2\left(2-\frac{c_2}{c_1}-\frac{c_1}{c_2}\right)\left(\frac{c_1}{c_2}\right)^2-\left(2\frac{c_2}{c_1}-1\right)\right)\left.\frac{\partial\xi_A}{\partial x}\right|_{x=0}\left.\frac{\partial\xi_B}{\partial x}\right|_{x=0}\frac{h_2}{c_1}\\
&+\left(3\left(\frac{c_2}{c_1}-1\right)^2\left(\left.\frac{\partial\xi_A}{\partial x}\right|_{x=0}\right)^2-2\frac{c_2}{c_1}\left.\frac{\partial\xi_A}{\partial x}\right|_{x=0}\left.\frac{\partial\xi_B}{\partial x}\right|_{x=0}+2\left(\left.\frac{\partial\xi_B}{\partial x}\right|_{x=0}\right)^2\right)\frac{h_2}{c_2}\\
&+O\left(\varepsilon^3\right).
\end{aligned} \tag{A6}$$

We define $\Delta t_A=t_A-2b/c_0$, $\Delta t_B=t_B-2b/c_0$. Therefore, the measurement errors for interface A and B are

$$\kappa_A=\xi_A-\frac{1}{2}c_1\Delta t_A,\quad \kappa_B=\xi_B-\left(\frac{1}{2}c_2\left(\Delta t_B-\Delta t_A\right)+\frac{1}{2}c_1\Delta t_A\right). \tag{A7}$$

https://doi.org/10.1017/jfm.2025.10562 Published online by Cambridge University Press

Furthermore, we derive the following approximate functions for the errors:

$$\kappa_A \sim -h_1\left(1+\frac{h_1}{b}\frac{c_1}{c_0}\right)\varepsilon^2,$$
$$\kappa_B \sim h_1\left(\left(\frac{c_2}{c_1}-1+\frac{h_1}{b}\left(\frac{c_2}{c_0}-\frac{c_1}{c_0}\right)\right)-\frac{1}{4}\frac{c_2}{c_0}\frac{h_1}{b}\left(\left(\frac{c_2}{c_1}-1\right)\left(\frac{c_2}{c_1}-3\right)+2\frac{c_1}{c_2}\right)^2\right.$$
$$\left.-\frac{c_2}{c_1}\left(2-\frac{c_2}{c_1}\right)^2\right)\varepsilon^2-h_2\frac{c_2}{c_1}\left(2-\frac{1}{2}\frac{c_2}{c_1}+\frac{c_1}{c_2}\left(2-\frac{c_2}{c_1}-\frac{c_1}{c_2}\right)+\left(2-\frac{c_2}{c_1}-\frac{c_1}{c_2}\right)^2\right.$$
$$\left.+\left(\frac{c_1}{c_2}\right)^2\right)\varepsilon^2-\frac{1}{2}h_2\left(3\left(\frac{c_2}{c_1}\right)^2-8\frac{c_2}{c_1}+5\right)\varepsilon^2. \tag{A8}$$

Next, considering the order of magnitude of the parameters used in this study, $\varepsilon\sim 0.05$, $h_1, h_2\sim 30\,\mathrm{mm}$, $b\sim 20\,\mathrm{mm}$, $c_0=2700\,\mathrm{m\,s^{-1}}$, $c_1=960\,\mathrm{m\,s^{-1}}$, $c_2=1300\,\mathrm{m\,s^{-1}}$, we substitute them into the expression for the error function to obtain the following approximate values for the measurement errors:

$$|\kappa_A|\approx 0.12\,\mathrm{mm},\quad |\kappa_B|\approx 0.19\,\mathrm{mm}. \tag{A9}$$

Therefore, we can calculate position of interface A and B with $\xi_A\approx c_1\Delta t_A/2$, $\xi_B\approx c_2(\Delta t_B-\Delta t_A)/2+c_1\Delta t_A/2$, whose errors are $|\kappa_A|$ and $|\kappa_B|$ approximately.

Appendix B. BOS in three-layer fluid systems

As shown in figure 12(*a*), we define I_B as the point where the optical path intersects with interface B, and I_A as the point where the optical path intersects with interface A. Additionally, M_B'' is the intersection of the extension of CI_B with the bottom and M_A'' is the intersection of the extension of I_BI_A with the bottom. Line OE is perpendicular to line EM_B'', where EM_B'' is the intersection line of the plane CEM_B'' with the bottom plane. Line OF is perpendicular to FM_A'', where FM_A'' is the intersection line of the plane I_BFM_A'' with the bottom plane. Based on geometric relationships, point M (intersection of the optical path with the bottom) lies on the segment FM_A''. We proceed with the derivation under the assumption of small angles, $i_A, i_B, \theta_A, \theta_B\sim 0$ (Moisy *et al.* 2009).

In the plane CEM_B'' (figure 12*b*), based on geometric relationships, the outward normal direction of interface B satisfies the geometric relationship,

$$\hat{n}_B=i_B\hat{s}_B-\frac{\overrightarrow{CM_B''}}{|CM_B''|}. \tag{B1}$$

From the law of refraction,

$$\overrightarrow{M_A''M_B''}=\alpha_B\xi_Bi_B\hat{s}_B, \tag{B2}$$

where $\alpha_B=1-n_B/n_B'$. Based on the assumption of small angles, $|CM_B''|\sim H$, $|OM_B''|\sim 0$, where H is the length of line segment OC. According to (B1), (B2), under the assumption of small angles, the wave height gradient field of interface B is satisfied,

$$\nabla h_B=\frac{\overrightarrow{OM_B''}}{H}-i_B\frac{\overrightarrow{M_A''M_B''}}{|M_A''M_B''|}\approx-\frac{\overrightarrow{M_A''M_B''}}{\alpha_B\,(h_1+h_2)}. \tag{B3}$$

https://doi.org/10.1017/jfm.2025.10562 Published online by Cambridge University Press

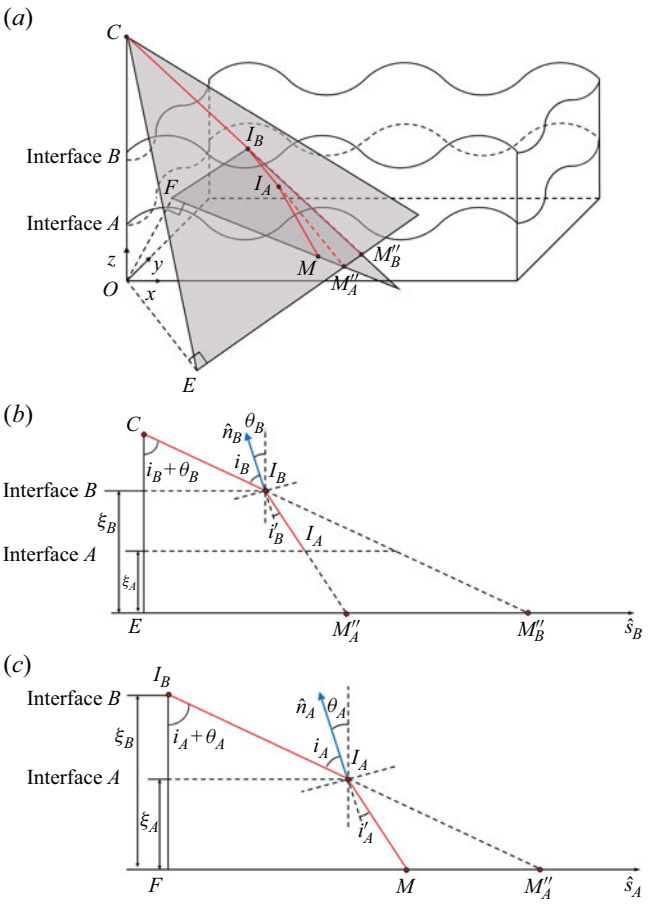


Figure 12. (*a*) Optical path diagram. The solid red line is the optical path and the dotted red line is the optical path extension cable. (*b*) Diagram of plane CEM''_B. (*c*) Diagram of plane $I_B F M''_A$.

In the plane $I_B F M''_A$ (figure 1*c*), based on geometric relationships, it is known that the outward normal direction of interface A satisfies the geometric relationship,

$$\hat{n}_A = i_A \hat{s}_A - \frac{\overrightarrow{I_B M''_A}}{\left|I_B M''_A\right|}. \tag{B4}$$

From the law of refraction,

$$\overrightarrow{MM''} = \alpha_A \xi_A i_A \hat{s}_A, \tag{B5}$$

where $\alpha_A = 1 - n_A/n'_A$. Based on the assumption of small angles, $\left|I_B M''_A\right| \sim \xi_B$, $\left|O M''_A\right| \sim 0$. According to (B4), (B5), under the assumption of small angles, the wave height gradient field of interface A is satisfied such that

$$\nabla \xi_A = \frac{\overrightarrow{O M''_A}}{\xi_B} - i_A \frac{\overrightarrow{MM''_A}}{\left|M M''_A\right|} \approx -\frac{\overrightarrow{MM''_A}}{\alpha_A h_1}. \tag{B6}$$

https://doi.org/10.1017/jfm.2025.10562 Published online by Cambridge University Press

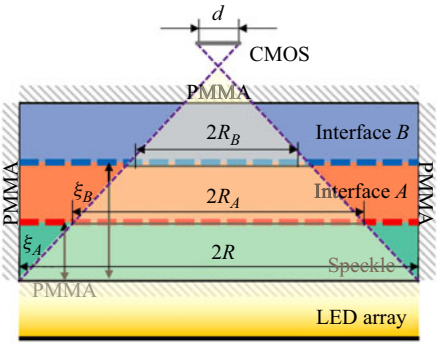


Figure 13. Schematic diagram of the imaging region.

From geometry, we know

$$\overrightarrow{MM_B''} = \overrightarrow{MM_A''} + \overrightarrow{M_A''M_B''}. \tag{B7}$$

Substituting (B3), (B6) into (B7) and simplifying, we obtain

$$\delta \boldsymbol{r} = \overrightarrow{MM_B''} = -\left(\alpha_A h_1 \nabla \xi_A + \alpha_B \left(h_1 + h_2\right) \nabla \xi_B\right). \tag{B8}$$

Hence, the speckle displacements obtained through image autocorrelation correspond to a weighted average of the gradients of the two interfaces, with the weighting coefficients dependent on the refractive indices and fluid depths. According to the principles of the camera, the BOS images obtained in the experiment are formed by the superposition of waves in the shaded region shown in figure 13. Therefore, the actual speckle displacement is given by

$$\delta \boldsymbol{r} = -\left(\alpha_A h_1 \nabla \xi_A \left(r R_A / R\right) + \alpha_B \left(h_1 + h_2\right) \nabla \xi_B \left(r R_B / R\right)\right), \quad 0 \leqslant r \leqslant R, \tag{B9}$$

where $R_A = R - h_1 d/(2f)$, $R_B = R - (h_1 + h_2)d/(2f)$, f is the focal length of the lens and d is the size of the CMOS imaging area.

Appendix C. Full hydrodynamic equations

The incompressible continuity and N-S momentum equations are

$$\nabla \cdot \boldsymbol{v}_j = 0, \tag{C1a}$$

$$\frac{\partial \boldsymbol{v}_j}{\partial t} + \left(\boldsymbol{v}_j \cdot \nabla\right) \boldsymbol{v}_j + \frac{1}{\rho_j} \nabla P_j - g + \dot{\boldsymbol{V}}_0 - \nu_j \nabla^2 \boldsymbol{v}_j = 0, \tag{C1b}$$

and boundary conditions

$$\text{Wall}: \quad \boldsymbol{v}_j\big|_{z=0} \big\|_{z=\sum_1^3 h_j} \big\|_{r=R} = 0, \tag{C2a}$$

$$\text{Interface } A: \quad \boldsymbol{v}_1 \cdot \boldsymbol{n}_A|_{z=\xi_A} = \boldsymbol{v}_2 \cdot \boldsymbol{n}_A|_{z=\xi_A} = \frac{\partial \xi_A}{\partial t} + \left(\boldsymbol{v}_j \cdot \nabla\right) \xi_A\big|_{z=h_1+\eta_A}, \tag{C2b}$$

$$\boldsymbol{v}_1 \cdot \boldsymbol{t}_A|_{z=\xi_A} = \boldsymbol{v}_2 \cdot \boldsymbol{t}_A|_{z=\xi_A}, \tag{C2c}$$

https://doi.org/10.1017/jfm.2025.10562 Published online by Cambridge University Press

$$\boldsymbol{n}_A \cdot \left(\tau_{1,ls} - \tau_{2,ls}\right) \cdot \boldsymbol{n}_A\big|_{z=\xi_A} = \sigma_A \nabla \cdot \frac{\nabla \xi_A}{\sqrt{1+|\nabla \xi_A|^2}}, \tag{C2d}$$

$$\boldsymbol{n}_A \cdot \left(\tau_{1,ls} - \tau_{2,ls}\right) \cdot \boldsymbol{t}_A\big|_{z=\xi_A} = 0, \tag{C2e}$$

Interface B :

$$\boldsymbol{v}_2 \cdot \boldsymbol{n}_B|_{z=\xi_A} = \boldsymbol{v}_3 \cdot \boldsymbol{n}_B|_{z=\xi_A} = \frac{\partial \xi_B}{\partial t} + \left(\boldsymbol{v}_j \cdot \nabla\right) \xi_B\big|_{z=h_1+h_2+\xi_A}, \tag{C2f}$$

$$\boldsymbol{v}_2 \cdot \boldsymbol{t}_B|_{z=\xi_A} = \boldsymbol{v}_3 \cdot \boldsymbol{t}_B|_{z=\xi_A}, \tag{C2g}$$

$$\boldsymbol{n}_B \cdot \left(\tau_{2,ls} - \tau_{3,ls}\right) \cdot \boldsymbol{n}_B\big|_{z=\xi_B} = \sigma_B \nabla \cdot \frac{\nabla \xi_B}{\sqrt{1+|\nabla \xi_B|^2}}, \tag{C2h}$$

$$\boldsymbol{n}_B \cdot \left(\tau_{2,ls} - \tau_{3,ls}\right) \cdot \boldsymbol{t}_B\big|_{z=h_1+h_2+\xi_B} = 0, \tag{C2i}$$

where $\boldsymbol{n}$ and $\boldsymbol{t}$ are the outward-directed unit normal vector and unit tangential vector at an interface.

Appendix D. Solutions of the modified model

The full solution of the modified model is given by

$$\eta_A(r,\phi) = \sum_{n=1}^{\infty} \frac{J_1\left(k_{1,n} r\right)}{J_1\left(k_{1,n} R\right)} \left(\beta_{A,C,n} \cos\phi + \beta_{A,S,n} \sin\phi\right),$$

$$\eta_B(r,\phi) = \sum_{n=1}^{\infty} \frac{J_1\left(k_{1,n} r\right)}{J_1\left(k_{1,n} R\right)} \left(\beta_{B,C,n} \cos\phi + \beta_{B,S,n} \sin\phi\right), \tag{D1}$$

where

$$\begin{aligned}
\beta_{A,C,n} = {} & d_s \kappa_n \left(2\frac{\lambda}{\Omega} F_{B,n} \rho_{A,n} \left(4\frac{\lambda^2}{\Omega^2}\left(\rho_{A,n}\rho_{B,n} - 1\right) + \left(\rho_{A,n}\rho_{B,n} - 1\right) + \frac{\Omega_{A,n}^2 \Omega_{B,n}^2}{\Omega^4}\right)\right) \\
& + d_s \kappa_n \left(2\frac{\lambda}{\Omega} F_{A,n} \left(4\frac{\lambda^2}{\Omega^2}\left(\rho_{A,n}\rho_{B,n} - 1\right) + \left(\rho_{A,n}\rho_{B,n} - 1\right)\right.\right. \\
& \left.\left. -2\left(\rho_{A,n}\rho_{B,n} - 1\right)\frac{\Omega_{B,n}^2}{\Omega^2} - \frac{\Omega_{B,n}^4}{\Omega^4}\right)\right) \\
\beta_{A,S,n} = {} & -d_s \kappa_n \left(F_{B,n} \rho_{A,n} \left(-\gamma_n + 4\frac{\lambda^2}{\Omega^2}\left(\left(\rho_{A,n}\rho_{B,n} - 1\right) + \frac{\Omega_{A,n}^2}{\Omega^2} + \frac{\Omega_{B,n}^2}{\Omega^2}\right)\right)\right) \\
& - d_s \kappa_n \left(F_{A,n} \left(4\frac{\lambda^2}{\Omega^2}\left(\left(\rho_{A,n}\rho_{B,n} - 1\right) + \frac{\Omega_{A,n}^2}{\Omega^2} + \rho_{A,n}\rho_{B,n}\frac{\Omega_{B,n}^2}{\Omega^2}\right)\right.\right. \\
& \left.\left. - \left(1 - \frac{\Omega_{B,n}^2}{\Omega^2}\right)\gamma_n\right)\right), \\
\beta_{B,C,n} = {} & d_s \kappa_n \left(2\frac{\lambda}{\Omega} F_{A,n} \rho_{B,n} \left(4\frac{\lambda^2}{\Omega^2}\left(\rho_{A,n}\rho_{B,n} - 1\right) + \left(\rho_{A,n}\rho_{B,n} - 1\right) + \frac{\Omega_{A,n}^2 \Omega_{B,n}^2}{\Omega^4}\right)\right) \\
& + d_s \kappa_n \left(2\frac{\lambda}{\Omega} F_{B,n} \left(4\frac{\lambda^2}{\Omega^2}\left(\rho_{A,n}\rho_{B,n} - 1\right) + \left(\rho_{A,n}\rho_{B,n} - 1\right)\right.\right. \\
& \left.\left. -2\left(\rho_{A,n}\rho_{B,n} - 1\right)\frac{\Omega_{A,n}^2}{\Omega^2} - \frac{\Omega_{A,n}^4}{\Omega^4}\right)\right)
\end{aligned}$$

https://doi.org/10.1017/jfm.2025.10562 Published online by Cambridge University Press

$$\beta_{B,S,n} = -d_s\kappa_n\left(F_{A,n}\rho_{B,n}\left(-\gamma_n + 4\frac{\lambda^2}{\Omega^2}\left(\left(\rho_{A,n}\rho_{B,n}-1\right) + \frac{\Omega_{A,n}^2}{\Omega^2} + \frac{\Omega_{B,n}^2}{\Omega^2}\right)\right)\right)$$
$$- d_s\kappa_n\left(F_{B,n}\left(4\frac{\lambda^2}{\Omega^2}\left(\left(\rho_{A,n}\rho_{B,n}-1\right) + \frac{\Omega_{B,n}^2}{\Omega^2} + \rho_{A,n}\rho_{B,n}\frac{\Omega_{A,n}^2}{\Omega^2}\right)\right.\right.$$
$$\left.\left. - \left(1 - \frac{\Omega_{A,n}^2}{\Omega^2}\right)\gamma_n\right)\right), \tag{D2}$$

with

$$\frac{1}{\kappa_n} = 16\left(\rho_{A,n}\rho_{B,n}-1\right)^2\frac{\lambda^4}{\Omega^4} + \gamma_n^2 + 4\frac{\lambda^2}{\Omega^2}\left(2\left(\rho_{A,n}\rho_{B,n}-1\right)\left(1 + \frac{\Omega_{A,n}^2}{\Omega^2} + \frac{\Omega_{B,n}^2}{\Omega^2}\right)\right.$$
$$\left. + 2\rho_{A,n}\rho_{B,n}\frac{\Omega_{A,n}^2}{\Omega^2}\frac{\Omega_{B,n}^2}{\Omega^2} + \frac{\Omega_{A,n}^4}{\Omega^4} + \frac{\Omega_{B,n}^4}{\Omega^4}\right),$$
$$\gamma_n = 1 - \rho_{A,n}\rho_{B,n} + \frac{\Omega_{A,n}^2}{\Omega^2}\frac{\Omega_{B,n}^2}{\Omega^2} - \left(\frac{\Omega_{A,n}^2}{\Omega^2} + \frac{\Omega_{B,n}^2}{\Omega^2}\right). \tag{D3}$$

For the inviscid fluid system, $\beta_{A,C,n} = 0$, indicating no phase difference between the interface wave amplitude and the tank oscillation. When fluid viscosity is considered, $\beta_{A,C,n} \neq 0$, and a phase difference arises between the interface and the oscillating tank.

In addition, $\gamma_n = 0$ is equivalent to

$$\rho_{A,n}\rho_{B,n} = \frac{\left(\omega^2 - \Omega_{A,n}^2\right)\left(\omega^2 - \Omega_{B,n}^2\right)}{\Omega^4}. \tag{D4}$$

As $\gamma_n = 0$, Ω equals resonance frequency of the three-layer inviscid fluid system (Huang *et al.* 2024).

The asymptotic solution far from resonance is

$$\beta_{A,S,n} = \frac{d_s}{\gamma_n\Omega^2}\left(\left(F_{A,n} + \rho_{A,n}F_{B,n}\right)\Omega^2 - d_sF_{A,n}\Omega_{B,n}^2\right) + O\left(\Upsilon^2\right),$$
$$\beta_{A,C,n} = \frac{2d_s\Upsilon}{\gamma_n^2\Omega^4}F_{A,n}\rho_{B,n}\left(\left(-1 + \rho_{A,n}\rho_{B,n}\right)\Omega^4 + \Omega_{A,n}^2\Omega_{B,n}^2\right)$$
$$+ \frac{2d_s\Upsilon}{\gamma_n^2\Omega^4}F_{B,n}\left(\left(-1 + \rho_{A,n}\rho_{B,n}\right)\Omega^4 - 2\left(-1 + \rho_{A,n}\rho_{B,n}\right)\Omega^2\Omega_{A,n}^2 - \Omega_{A,n}^4\right)$$
$$+ O\left(\Upsilon^2\right),$$
$$\beta_{B,S,n} = \frac{d_s}{\gamma_n\Omega^2}\left(\left(F_{B,n} + \rho_{B,n}F_{A,n}\right)\Omega^2 - d_sF_{B,n}\Omega_{A,n}^2\right) + O\left(\Upsilon^2\right),$$
$$\beta_{B,C,n} = \frac{2d_s\Upsilon}{\gamma_n^2\Omega^4}F_{B,n}\rho_{A,n}\left(\left(-1 + \rho_{A,n}\rho_{B,n}\right)\Omega^4 + \Omega_{A,n}^2\Omega_{B,n}^2\right)$$
$$+ \frac{2d_s\Upsilon}{\gamma_n^2\Omega^4}F_{A,n}\left(\left(-1 + \rho_{A,n}\rho_{B,n}\right)\Omega^4 - 2\left(-1 + \rho_{A,n}\rho_{B,n}\right)\Omega^2\Omega_{B,n}^2 - \Omega_{B,n}^4\right)$$
$$+ O\left(\Upsilon^2\right). \tag{D5}$$

https://doi.org/10.1017/jfm.2025.10562 Published online by Cambridge University Press

The asymptotic solution at resonance is

$$\beta_{A,S,n} = \frac{\begin{array}{c} d_s\Omega^2\Big(-\Big((F_{A,n}+F_{B,n}\rho_{A,n})\Big((-1+\rho_{A,n}\rho_{B,n})\Omega^2+\Omega_{A,n}^2\Big)\Big) \\ -\rho_{A,n}(F_{B,n}+F_{A,n}\rho_{B,n})\Omega_{B,n}^2\Big) \end{array}}{\begin{array}{c} 2(-1+\rho_{A,n}\rho_{B,n})^2\Omega^4+\Omega_{A,n}^4+2\rho_{A,n}\rho_{B,n}\Omega_{A,n}^2\Omega_{B,n}^2 \\ +\Omega_{B,n}^4+2(-1+\rho_{A,n}\rho_{B,n})\Omega^2\left(\Omega_{A,n}^2+\Omega_{B,n}^2\right) \end{array}} + O(\Upsilon),$$

$$\beta_{A,C,n} = \Upsilon^{-1}\frac{d_s}{2}\frac{\begin{array}{c} \left(F_{A,n}\rho_{B,n}\left(-1+\rho_{A,n}\rho_{B,n}+\frac{\Omega_{A,n}^2}{\Omega^2}\frac{\Omega_{B,n}^2}{\Omega^2}\right)\right. \\ \left.+F_{B,n}\left((-1+\rho_{A,n}\rho_{B,n})\left(1-2\frac{\Omega_{A,n}^2}{\Omega^2}\right)-\frac{\Omega_{A,n}^4}{\Omega^4}\right)\right) \end{array}}{\begin{array}{c} 2(-1+\rho_{A,n}\rho_{B,n})^2+2(-1+\rho_{A,n}\rho_{B,n})\left(\frac{\Omega_{A,n}^2}{\Omega^2}+\frac{\Omega_{B,n}^2}{\Omega^2}\right) \\ +2\rho_{A,n}\rho_{B,n}\frac{\Omega_{A,n}^2}{\Omega^2}\frac{\Omega_{B,n}^2}{\Omega^2}+\frac{\Omega_{A,n}^4}{\Omega^4}+\frac{\Omega_{B,n}^4}{\Omega^4} \end{array}} + O(\Upsilon),$$

$$\beta_{B,S,n} = \frac{\begin{array}{c} d_s\Omega^2\Big(-\Big((F_{B,n}+F_{A,n}\rho_{B,n})\Big((-1+\rho_{A,n}\rho_{B,n})\Omega^2+\Omega_{B,n}^2\Big)\Big) \\ -\rho_{B,n}(F_{A,n}+F_{B,n}\rho_{A,n})\Omega_{A,n}^2\Big) \end{array}}{\begin{array}{c} 2(-1+\rho_{A,n}\rho_{B,n})^2\Omega^4+\Omega_{A,n}^4+2\rho_{A,n}\rho_{B,n}\Omega_{A,n}^2\Omega_{B,n}^2 \\ +\Omega_{B,n}^4+2(-1+\rho_{A,n}\rho_{B,n})\Omega^2\left(\Omega_{A,n}^2+\Omega_{B,n}^2\right) \end{array}} + O(\Upsilon),$$

$$\beta_{B,C,n} = \Upsilon^{-1}\frac{d_s}{2}\frac{\begin{array}{c} \left(F_{B,n}\rho_{A,n}\left(-1+\rho_{A,n}\rho_{B,n}+\frac{\Omega_{B,n}^2}{\Omega^2}\frac{\Omega_{A,n}^2}{\Omega^2}\right)\right. \\ \left.+F_{A,n}\left((-1+\rho_{A,n}\rho_{B,n})\left(1-2\frac{\Omega_{B,n}^2}{\Omega^2}\right)-\frac{\Omega_{B,n}^4}{\Omega^4}\right)\right) \end{array}}{\begin{array}{c} 2(-1+\rho_{A,n}\rho_{B,n})^2+2(-1+\rho_{A,n}\rho_{B,n})\left(\frac{\Omega_{A,n}^2}{\Omega^2}+\frac{\Omega_{B,n}^2}{\Omega^2}\right) \\ +2\rho_{A,n}\rho_{B,n}\frac{\Omega_{A,n}^2}{\Omega^2}\frac{\Omega_{B,n}^2}{\Omega^2}+\frac{\Omega_{A,n}^4}{\Omega^4}+\frac{\Omega_{B,n}^4}{\Omega^4} \end{array}} + O(\Upsilon).$$

(D6)

References

Abramson, H.N. 1966 The dynamic behavior of liquids in moving containers, with applications to space vehicle technology. Tech. Rep.

Batson, W., Zoueshtiagh, F. & Narayanan, R. 2013 The Faraday threshold in small cylinders and the sidewall non-ideality. *J. Fluid Mech.* **729**, 496–523.

Bauer, H.F. & Eidel, W. 1999 Axisymmetric natural damped frequencies of a viscous liquid in a circular cylindrical container – an alternative semi-analytical solution. *Forsch. Ing.* **65** (7), 191–199.

Bisswanger, S., Bonart, H., Khaing, P.T. & Hardt, S. 2024 Liquid surfaces with chaotic capillary waves exhibit an effective surface tension. *Phys. Rev. Lett.* **133** (3), 034001.

Bongarzone, A. & Gallaire, F. 2024 Lagrangian versus Eulerian view on the mean drift and streaming flows in orbital sloshing. *Phys. Rev. Fluids* **9**, 124803.

Bongarzone, A., Guido, M. & Gallaire, F. 2022 An amplitude equation modelling the double-crest swirling in orbital-shaken cylindrical containers. *J. Fluid Mech.* **943**, A28.

Chen, P., Ghassemi-Armaki, H., Kumar, S., Bower, A., Bhat, S. & Sadagopan, S. 2014 Microscale-calibrated modeling of the deformation response of dual-phase steels. *Acta Mater.* **65**, 133–149.

Dodge, F.T. *et al.* 2000 *The new dynamic behavior of liquids in moving containers*. Southwest Research Institution.

https://doi.org/10.1017/jfm.2025.10562 Published online by Cambridge University Press

EKMAN, V.W. 1904 On dead water, norw. n. polar exped. PhD thesis.
FALTINSEN, O.M. & TIMOKHA, A.N. 2009 *Sloshing*. Cambridge University Press.
FOURDRINOY, J., DAMBRINE, J., PETCU, M., PIERRE, M. & ROUSSEAUX, G. 2020 The dual nature of the dead-water phenomenology: Nansen versus Ekman wave-making drags. *Proc. Natl Acad. Sci.* **117** (29), 16770–16775.
GONG, QI., HUANG, Y.-F., YANG, J.-C. & NI, M.-J. 2025 Faraday instability of a three-layer fluid system in a Hele-Shaw cell: Transition from zigzag mode to B-interface instability mode. *Phys. Rev. Fluids* **10**, 024005.
GUEX, A.G., DI MARZIO, N., EGLIN, D., ALINI, M. & SERRA, T. 2021 The waves that make the pattern: a review on acoustic manipulation in biomedical research. *Mater. Today Bio.* **10**, 100110.
HERREMAN, W., NORE, C., GUERMOND, J.-L., CAPPANERA, L., WEBER, N. & HORSTMANN, G.M. 2019 Perturbation theory for metal pad roll instability in cylindrical reduction cells. *J. Fluid Mech.* **878**, 598–646.
HERREMAN, W., WIERZCHALEK, L., HORSTMANN, G.M., CAPPANERA, L. & NORE, C. 2023 Stability theory for metal pad roll in cylindrical liquid metal batteries. *J. Fluid Mech.* **962**, A6.
HORSTMANN, G.M. 2021 Multilayer interfacial wave dynamics in upright circular cylinders with application to liquid metal batteries. *PhD thesis*, Helmholtz–Zentrum Dresden–Rossendorf, Germany.
HORSTMANN, G.M., ANDERS, S., KELLEY, D.H. & WEIER, T. 2021 Formation of spiral waves in cylindrical containers under orbital excitation. *J. Fluid Mech.* **925**, A28.
HORSTMANN, G.M., HERREMAN, W. & WEIER, T. 2020 Linear damped interfacial wave theory for an orbitally shaken upright circular cylinder. *J. Fluid Mech.* **891**, A22.
HORSTMANN, G.M., WEBER, N. & WEIER, T. 2018 Coupling and stability of interfacial waves in liquid metal batteries. *J. Fluid Mech.* **845**, 1–35.
HORSTMANN, G.M., WYLEGA, M. & WEIER, T. 2019 Measurement of interfacial wave dynamics in orbitally shaken cylindrical containers using ultrasound pulse-echo techniques. *Exp. Fluids* **60**, 1–17.
HUANG, Y.-F., ZHUO, R.-L., YANG, J.-C. & NI, M.-J. 2024 Interface coupling effect and multi-mode Faraday instabilities in a three-layer fluid system. *J. Fluid Mech.* **982**, A8.
IBRAHIM, R.A. 2005 *Liquid Sloshing Dynamics: Theory and Applications*. Cambridge University Press.
KELLEY, D.H. & WEIER, T. 2018 Fluid mechanics of liquid metal batteries. *Appl. Mech. Rev.* **70** (2), 020801.
KIYASHKO, S.V., KORZINOV, L.N., RABINOVICH, M.I. & TSIMRING, L.SH 1996 Rotating spirals in a Faraday experiment. *Phys. Rev. E* **54** (5), 5037.
KLÖCKNER, W. & BÜCHS, J. 2012 Advances in shaking technologies. *Trends Biotechnol.* **30** (6), 307–314.
KLÖCKNER, W., DIEDERICHS, S. & BÜCHS, J. 2014 *Orbitally shaken single-use bioreactors*. Disposable Bioreactor II, pp. 45–60.
KUMAR, K. & TUCKERMAN, L.S. 1994 Parametric instability of the interface between two fluids. *J. Fluid Mech.* **279**, 49–68.
LIU, D., WU , Y. & LIN , P. 2022 The interfacial swirling motion of two-layer liquids in a tank under orbital excitations. *Phys. Fluids* **34** (11), 112109.
LIU, Z., JIANG, J., JIN, X., WANG, Y. & ZHANG, Y. 2023 Experimental and numerical investigations on the inhibition of freeze–thaw damage of cement-based materials by a methyl laurate/diatomite microcapsule phase change material. *J. Energy Storage* **68**, 107665.
MARCOTTE, A., GALLAIRE, F. & BONGARZONE, A. 2023 Super-harmonically resonant swirling waves in longitudinally forced circular cylinders. *J. Fluid Mech.* **966**, A41.
MERCIER, M.J., VASSEUR, R. & DAUXOIS, T. 2011 Resurrecting dead-water phenomenon. *Nonlinear Proc. Geophys.* **18** (2), 193–208.
MOISY, F., RABAUD, M. & SALSAC, K. 2009 A synthetic Schlieren method for the measurement of the topography of a liquid interface. *Exp. Fluids* **46** (6), 1021–1036.
PAN, D.-Y., HUANG, Y.-F., LYU, Z., YANG, J.-C. & NI, M.-J. 2025 Verification of the multichannel pulsed ultrasonic Doppler velocimeter for the measurement of liquid metal flow. *Exp. Fluids* **66** (3), 61.
PUCCI, G., FORT, E., BEN AMAR, M. & COUDER, Y. 2011 Mutual adaptation of a Faraday instability pattern with its flexible boundaries in floating fluid drops. *Phys. Rev. Lett.* **106** (2), 024503.
RECLARI, M., DREYER, M., TISSOT, S., OBRESCHKOW, D., WURM, F.M. & FARHAT, M. 2014 Surface wave dynamics in orbital shaken cylindrical containers. *Phys. Fluids* **26** (5), 052104.
SHAO, X., WILSON, P., SAYLOR, J.R. & BOSTWICK, J.B. 2021 Surface wave pattern formation in a cylindrical container. *J. Fluid Mech.* **915**, A19.
VIOLA, F., GALLAIRE, F. & DOLLET, B. 2017 Sloshing in a Hele–Shaw cell: experiments and theory. *J. Fluid Mech.* **831** (R1).
WARD, K., ZOUESHTIAGH, F. & NARAYANAN, R. 2019*a* Faraday instability in double-interface fluid layers. *Phys. Rev. Fluids* **4** (4), 043903.

https://doi.org/10.1017/jfm.2025.10562 Published online by Cambridge University Press

WARD, K., ZOUESHTIAGH, F. & NARAYANAN, R. 2019*b* The Faraday instability in rectangular and annular geometries: comparison of experiments with theory. *Exp. Fluids* **60** (4), 53.
WARD, K., ZOUESHTIAGH, F. & NARAYANAN, R. 2019*c* The Faraday instability in rectangular and annular geometries: comparison of experiments with theory. *Exp. Fluids* **60**, 1–10.

https://doi.org/10.1017/jfm.2025.10562 Published online by Cambridge University Press